Langtaosha (LTS) Preprint doi: https://doi.org/10.65215/LTSpreprints.2026.04.18.000189. This version posted April 18, 2026. The copyright holder for this preprint (which was not certified by peer review) is the author/funder. Creative Commons license: CC Attribution-NonCommercial-NoDerivatives 4.0 https://creativecommons.org/licenses/by-nc-nd/4.0

A conserved helix-tiling architecture of urate oxidase organizes metabolism in peroxisomes

Junhan Yang[1, *], Zhe Chen[1, *], Yonglun Wang[2, *], Zibo Yu[1], Sihao Yuan[3], Xiao Sun[4, 5], Chuanwen Kan[4, 5], Wenjing Du[1], Zhixun Li[1], Shenjia Luo[1], Yuan'gang Zhu[2], Xinyang Shao[6, 7], Guanbo Wang[6], Mingkun Li[4, 5], Yiqin Gao[3], Xiaowei Chen[2, #], Qiang Guo[1, 7, #].

[1]State Key Laboratory of Membrane Biology, Peking-Tsinghua Joint Center for Life Sciences, Scholar of Life Sciences, Peking University, Beijing 100871, China

[2]State Key Laboratory of Membrane Biology and Institute of Molecular Medicine, College of Future Technology, Peking University, Beijing 100871, China

[3]College of Chemistry and Molecular Engineering, Peking University, Beijing 100871, China

[4]Beijing Institute of Genomics, Chinese Academy of Sciences, and China National Center for Bioinformation, Beijing, China

[5]University of Chinese Academy of Sciences, Beijing, China

[6]Biomedical Pioneering Innovation Center (BIOPIC), Peking University, Beijing 100871, China

[7]Changping Laboratory, Beijing 102206, China

* Equal contribution

Co-correspondence

Lead contact: guo.qiang@pku.edu.cn

Langtaosha (LTS) Preprint doi: https://doi.org/10.65215/LTSpreprints.2026.04.18.000189. This version posted April 18, 2026. The copyright holder for this preprint (which was not certified by peer review) is the author/funder. Creative Commons license: CC Attribution-NonCommercial-NoDerivatives 4.0 https://creativecommons.org/licenses/by-nc-nd/4.0

Abstract

Cells organize metabolism within a crowded intracellular milieu, yet the structural logic and functional consequences of supramolecular enzyme assemblies *in vivo* remain poorly defined. Here, using *in situ* cryo-electron tomography, we identify a previously uncharacterized high-order architecture of urate oxidase in mouse liver. Urate oxidase homotetramers assemble into helical fibers that tile laterally to form a stable, and porous lamellar scaffold. This organization preserves extensive accessible surface area while permitting efficient substrate and product exchange. Structure-guided perturbation abolishes the assembly *in vivo* without measurably altering intrinsic catalytic activity, indicating a primary role in spatial organization rather than allosteric regulation. Consistent with this, the assembled state enhances resistance to thermal, proteolytic and oxidative stress, supporting sustained activity in the peroxide-rich peroxisomal matrix. Conserved across mammals, this architecture reveals a strategy for metabolic compartmentalization that couples efficient catalysis to increased molecular robustness without the trade-off between supramolecular assembly and enzyme accessibility.

Langtaosha (LTS) Preprint doi: https://doi.org/10.65215/LTSpreprints.2026.04.18.000189. This version posted April 18, 2026. The copyright holder for this preprint (which was not certified by peer review) is the author/funder. Creative Commons license: CC Attribution-NonCommercial-NoDerivatives 4.0 https://creativecommons.org/licenses/by-nc-nd/4.0

Introduction

The biochemical landscape of living cells fundamentally differs from dilute *in vitro* systems due to extreme macromolecular crowding, in which proteins and other macromolecules occupy approximately 15-30% of the intracellular volume [1,2]. This dense environment reshapes the thermodynamics and kinetics of biological processes, altering molecular diffusion, interaction equilibria, and effective reaction rates [3-6]. Consequently, cellular biochemistry operates under physical constraints that cannot be inferred from dilute systems alone. Rather than constituting a simple "bag of macromolecules", the intracellular milieu exhibits sophisticated organizational principles that have evolved to optimize biochemical processes under these constraints [7]. Understanding these principles in their native context is essential, as both structure and function emerge from coupled effects of crowding and cellular regulation that cannot be fully reconstituted in purified systems.

Cells employ diverse compartmentalization strategies to organize their crowded interior, with the resulting physical state determined by the strength and specificity of intermolecular interactions. Weak, multivalent interactions drive liquid-liquid phase separation, forming dynamic biomolecular condensates [8,9]. These membraneless organelles serve critical functions including concentrating specific enzymes to enhance reactions, organizing chromatin to regulate gene expression, and sequestering damaged proteins during cellular stress [10,11]. In contrast, strong and specific interactions give rise to stable solid-like assemblies, including amyloid aggregates [12] and crystalline inclusions [13], such as insulin in pancreatic β-cell secretory granules or yeast proteasome storage granules, which primarily function as inactive molecular storage [14,15].

These organizational states exist along a dynamic continuum, with many systems exhibiting stimulus-responsive interconversion [16]. Metabolic enzymes exemplify this plasticity, assembling into liquid-like condensates filaments or other high-order structures in response to changes in cellular metabolic state [17-20]. Increasingly, such assemblies are understood not to enhance intrinsic catalytic chemistry, but to act

Langtaosha (LTS) Preprint doi: https://doi.org/10.65215/LTSpreprints.2026.04.18.000189. This version posted April 18, 2026. The copyright holder for this preprint (which was not certified by peer review) is the author/funder. Creative Commons license: CC Attribution-NonCommercial-NoDerivatives 4.0 https://creativecommons.org/licenses/by-nc-nd/4.0

through spatial organization—modulating effective diffusion distances, local concentrations, and enzyme stability in crowded environments [6]. Recent discoveries have further expanded this paradigm, revealing unexpected organizational geometries—including fractal assemblies observed *in vivo*, though their functional significance remains enigmatic [21]. Together, these observations highlight the need to characterize novel molecular assemblies that integrate catalytic activity with non-canonical high-order organization in native cellular contexts.

Advances in cryo-electron tomography now enable structural characterization of these assemblies at molecular resolution within cells, frequently revealing architectures and functional states divergent from those observed *in vitro* [22]. Here, we report the discovery of a previously uncharacterized supramolecular assembly within peroxisomes of mouse liver tissue. We identify its molecular composition, resolve its high-order architecture, define its assembly mechanism, assess its enzymatic properties *in situ*, and establish its evolutionary conservation across mammals. These findings expand our understanding of how cells organize metabolic enzymes in crowded intracellular environments and reveal a distinct principle by which high-order organization supports metabolic function without altering intrinsic catalytic activity.

Langtaosha (LTS) Preprint doi: https://doi.org/10.65215/LTSpreprints.2026.04.18.000189. This version posted April 18, 2026. The copyright holder for this preprint (which was not certified by peer review) is the author/funder. Creative Commons license: CC Attribution-NonCommercial-NoDerivatives 4.0 https://creativecommons.org/licenses/by-nc-nd/4.0

Results

An uncharacterized supramolecular assembly in mouse hepatic peroxisomes

We leveraged our recently developed workflow to resolve the subcellular architecture of hepatocytes in mouse liver (Supplementary Figure 1a). This approach enabled the visualization of numerous organelles and their inter-organelle interactions, consistent with the central metabolic role of the liver [23]. Unexpectedly, we frequently observed a large supramolecular assembly with a distinct periodic pattern within single-membrane-bound organelles (Figure 1a-b, Supplementary Figure 1b-g). This assembly comprised parallel filamentous elements spaced at regular intervals of ~4 or ~8 nm, with the number of filaments ranging from a few to several dozen (Figure 1e-f, Supplementary Figure 1i). In orthogonal views, these elements appeared as hollow tubular densities spaced at ~10 nm and oriented at an angle of ~144° (Figure 1c-d, Supplementary Figure 1h). Together, the filaments formed irregularly curved sheet-like structures, as revealed in the three-dimensional segmentation (Figure 1b, Supplementary Figure 1g). To our knowledge, this architecture represents a previously uncharacterized intracellular assembly.

Organelles containing these assemblies have diameters of around 0.3~0.6 μm (Figure 1k). Most harbored one or two such assemblies (Figure 1l), featured a dense lumen, and were frequently encircled by endoplasmic reticulum (Figure 1a, Supplementary Figure 1b-f), reminiscent of the hepatocyte-enriched wrappER-peroxisome contact sites [24]. Based on these morphological features, we identified these organelles as peroxisomes, which are ubiquitous in eukaryotic cells. Previous ultrastructural studies have described a “crystalloid core” in hepatic peroxisomes from several mammalian species [25-28], and multiple structural models have been proposed [29,30], however, none resemble the organization observed in our data.

To further characterize this assembly, we performed subtomogram averaging to determine its molecular architecture (Supplementary Figure 2a). The fundamental repeating unit consisted of three laterally associated helical fibers, with an overall width

Langtaosha (LTS) Preprint doi: https://doi.org/10.65215/LTSpreprints.2026.04.18.000189. This version posted April 18, 2026. The copyright holder for this preprint (which was not certified by peer review) is the author/funder. Creative Commons license: CC Attribution-NonCommercial-NoDerivatives 4.0 https://creativecommons.org/licenses/by-nc-nd/4.0

of ~425 Å (Figure 1g-h). Adjacent fibers exhibited a center-to-center spacing of ~115 Å and an inter-fiber angle of ~144° (Figure 1g-h), in close agreement with measurements directly from tomograms (Figure 1d). Each fiber formed a hollow tube with an inner diameter of ~35 Å and an outer diameter of ~210 Å, which adopted a right-handed double-helical configuration (Figure 1i-j, Supplementary Figure 3a). The asymmetric unit in each fiber adopted a hollow cylindrical structure with an outer diameter and height of ~75 Å. Application of helical symmetry yielded a reconstruction at 7.3 Å resolution for a single fiber, sufficient to resolve secondary structural features (Supplementary Figure 2b-c, Supplementary Table 1).

To identify the molecular components of the assembly, we retrieved AlphaFold2-predicted structures [31] of all peroxisomal proteins detected at high frequency by mass spectrometry [32]. These models were fitted into the density map of asymmetric unit of the fiber using DiffFit [33] and ranked by Q-scores [34] (Supplementary Table 2). Urate oxidase (UOX, or uricase) exhibited the highest-scoring fit, supported by strong correspondence between the predicted secondary structural elements and our experimental density map (Supplementary Figure 2d). UOX catalyzes the oxidation of uric acid to 5-hydroxyisourate, an intermediate in purine degradation [35,36]. It is predominantly expressed in hepatocytes, where it localizes to peroxisomes [37-39].

To validate this assignment, we recombinantly expressed and purified mouse UOX and determined its structure *in vitro* using single-particle cryo-electron microscopy, achieving resolutions of 2.79 Å in the apo state and 2.42 Å in the substrate-bound state (Supplementary Figure 4, Supplementary Table 2). The recombinant UOX formed a homotetramer that aligned precisely with the asymmetric unit of the *in situ* fiber (Figure 1m). We therefore concluded that the supramolecular assembly in peroxisomes is exclusively composed of UOX, consistent with prior implications of UOX enrichment in the “crystalloid core” of peroxisomes [40].

Molecular basis of the UOX assembly

Langtaosha (LTS) Preprint doi: https://doi.org/10.65215/LTSpreprints.2026.04.18.000189. This version posted April 18, 2026. The copyright holder for this preprint (which was not certified by peer review) is the author/funder. Creative Commons license: CC Attribution-NonCommercial-NoDerivatives 4.0 https://creativecommons.org/licenses/by-nc-nd/4.0

Although the *in situ* resolution was sufficient to establish the molecular identity of the assembly, elucidating the molecular interactions governing helical fiber formation required higher-resolution structural details. Inspired by recent *ex vivo* structural studies [41,42], we isolated peroxisomes from mouse liver and imaged them to resolve the UOX assembly structure using single-particle cryo-EM approach (Supplementary Figure 5a). The integrity of peroxisomes and native architecture of the UOX assembly were well preserved after isolation, as indicated by identical helical parameters, yielding a reconstruction of the helical fiber at 3.64 Å resolution (Supplementary Figure 5b-c, Supplementary Table 2). This map enabled atomic model building and detailed analysis of the interactions underlying helical assembly.

To analyze inter-tetramer interactions, each asymmetric unit of the fiber — corresponding to a UOX homotetramer — was assigned a unique index based on the two-start right-handed helical symmetry and computationally "unwound" into two dimensions for visualization (Figure 2a-b, Supplementary Figure 3a). In this scheme, each unit i engages six first-shell neighbors: i ± 2, i ± 3, and i ± 5, defining three distinct interaction interfaces (Supplementary Figure 3b). Interface A, formed between units i and i ± 5, is stabilized primarily by electrostatic interactions involving Asn123 residues (Figure 2c-d). Interface B, between i and i ± 3, lacks obvious stabilizing contacts and is notably positioned adjacent to the catalytic site. Interface C, between i and i ± 2, is the most extensive, and drives right-handed helical propagation. This interface features reciprocal electrostatic interactions between Arg202 of unit i and Asn148 of unit i ± 2, reflecting the centrosymmetric geometry of the assembly. Additional stabilization arises from potential hydrogen bonds between Arg82 of one tetramer and Ser100/Ser101 of its neighbor (Figure 2e-g), as well as a hydrophobic patch formed by paired Leu81, Leu274, and Ile275 (Figure 2h-i). Together, these findings indicate that Interface C mediates primary helical extension, while Interface A facilitates secondary strand crossover, collectively enabling the observed double-helical architecture.

Interestingly, the cross-section view of the helical fiber exhibits an apparent fivefold

Langtaosha (LTS) Preprint doi: https://doi.org/10.65215/LTSpreprints.2026.04.18.000189. This version posted April 18, 2026. The copyright holder for this preprint (which was not certified by peer review) is the author/funder. Creative Commons license: CC Attribution-NonCommercial-NoDerivatives 4.0 https://creativecommons.org/licenses/by-nc-nd/4.0

symmetry, which, according to crystallographic restriction theorem, precludes the formation of a space-filling crystal lattice. This observation is consistent with the absence of crystalline blocks and the presence of extended lamellar sheets within peroxisomes. Analysis of inter-fiber contacts uncovered a distinctive lateral propagation mechanism, in which adjacent helical fibers share a column of UOX homotetramers (Figure 3a). The D_2 symmetry of each homotetramer generates four equivalent copies of Interface C, allowing a single fiber to extend laterally in up to five distinct directions. However, steric hindrance at multi-fiber junctions prevents simultaneous extension into immediately adjacent paths, imposing a defined angular constraint (Figure 3b). Iterative application of these geometric rules gives rise to a single-layered, unbranched lamellar architecture within peroxisomes, which we term as "helix tiling assembly" (Figure 3c-d, Supplementary Video 1). In this organization, helical fibers associate laterally while prohibit from forming a continuous, space-filling crystal.

We conceptualized this hierarchical principle as the "Three Breeds All" model: each helical fiber nucleates two neighbors to form a tripartite unit, which then serves as the fundamental module for propagation of the lamellar network. Consistent with this model, projection of the unmasked subtomogram averaged density map revealed a tree-like fiber pattern with characteristic ~144° inter-fiber angles (Fig. 3e). Quantitative mapping of the helical fibers back into original tomograms confirmed this architecture, showing close agreement with our model predictions. On average, individual UOX assembly contained ~27 distinct fibers (Fig. 3f).

Evolution of the UOX assembly

Our structural data suggest that formation of UOX assembly is primarily governed by Interface C, or several short motifs within it. Consistent with this interpretation, we occasionally observed similar assemblies in recombinant UOX expressed in *E. coli* (Supplementary Figure 6a-b), indicating that the capacity for self-assembly is at least partially intrinsic to the protein. Degradation of purines to uric acid is conserved across

Langtaosha (LTS) Preprint doi: https://doi.org/10.65215/LTSpreprints.2026.04.18.000189. This version posted April 18, 2026. The copyright holder for this preprint (which was not certified by peer review) is the author/funder. Creative Commons license: CC Attribution-NonCommercial-NoDerivatives 4.0 https://creativecommons.org/licenses/by-nc-nd/4.0

metazoans, however, downstream uric acid metabolism varies markedly between species. Most mammals, with the notable exception of human and hominoid primates, express UOX in their liver [43]. Previous ultrastructural studies of hepatic peroxisomes from diverse mammals have reported the widespread presence of putative UOX-derived crystalloid inclusions, with species-dependent variation in overall morphology observed across mice and other larger mammals, including rats and pigs [28].

Motivated by these observations, we wondered whether the helix tiling assembly is conserved among UOX-expressing mammals. Multiple-sequence alignment of mammalian UOX proteins revealed that residues comprising Interface C are nearly invariant, with only limited substitutions at positions 81, 82, 148, 202 and 275 (Figure 4a). Among these, positions 81 and 82 show the greatest divergence in mice relative to other mammals (Figure 4a, Supplementary Figure 7). To directly assess whether these sequence differences affect assembly, we performed *in situ* cryo-ET and subtomogram averaging of UOX assemblies from porcine and rat liver. Both porcine and rat UOX assemblies closely recapitulated the structure in mice, exhibiting only minor differences in helical parameters, while retaining identical fundamental repeating units and lateral propagation rules (Figure 4b-g). These results indicate that the L81F and R82K—two major differences between mice and other mammals—do not disrupt UOX assembly. The previously reported morphological variability among these species may therefore reflect limitations of two-dimensional projection imaging rather than fundamental differences in three-dimensional assembly. Moreover, prior ultrastructural surveys of hepatic peroxisomes [28] strongly suggest that UOX from additional mammals, including bovine, sheep, rabbit, hamster, guinea pig, cat and dog, form similar assemblies. In these species, the N148S variant is conserved and substitutions at positions 202 (R202K) and 275 (I275V) preserve the physicochemical properties (Supplementary Figure 7). Together, these observations suggest that the molecular principles governing UOX assembly are conserved across most UOX-expressing mammals.

To evaluate conservation beyond mammals, we expanded our sequence analysis across

Langtaosha (LTS) Preprint doi: https://doi.org/10.65215/LTSpreprints.2026.04.18.000189. This version posted April 18, 2026. The copyright holder for this preprint (which was not certified by peer review) is the author/funder. Creative Commons license: CC Attribution-NonCommercial-NoDerivatives 4.0 https://creativecommons.org/licenses/by-nc-nd/4.0

Chordata. Phylogenetic comparison revealed substantial divergence in assembly-critical motifs outside mammals (Supplementary Figure 8a). Notably, several substitutions alter key physicochemical properties of Interface A and C, including L81K and I275S, which disrupt hydrophobic interactions, and N123D, which abolishes an electrostatic contact (Supplementary Figure 8a-b). This divergence suggests that the UOX assembly is not strictly preserved across broader Chordata lineages. This conclusion aligns with earlier studies reporting UOX as a soluble protein in the peroxisomal matrix of fish and amphibians, in contrast to the insoluble crystalloid forms observed in more evolutionarily derived mammals [44-46]. Collectively, these findings indicate that the UOX assembly represents a mammal-specific structural adaptation rather than a universally conserved feature of uric acid metabolism.

Function of the UOX assembly

We next investigated the functional significance of UOX assembly formation. To assess its physiological prevalence, we performed pelleting assays on mouse hepatic peroxisome extracts, which revealed that over 90% of endogenous UOX partitions into the assembly fraction (Supplementary Figure 5l-m). This observation indicates that the assembly form represents the dominant intracellular state of UOX, which is probably a functional state rather than an inactive storage pool. To evaluate whether assembly formation modulates enzymatic activity, we compared the catalytic properties of the UOX assembly isolated from liver extracts with that of purified homotetramers. The UOX assembly retained robust catalytic activity, exhibiting only subtle differences to tetramers (Figure 5a). Such minimal effects are inconsistent with canonical allosteric regulation, in which high-order assembly typically accompanied by conformational rearrangements that substantially alter enzyme activity [21,47,48].

Structural and computational analyses further support this conclusion. First, assembly formation induces no major conformational changes: the root-mean-square deviation (RMSD) of all residues between free UOX tetramers and those forming assembly remained below 3.0 Å (Supplementary Figure 5k). Second, quantum

Langtaosha (LTS) Preprint doi: https://doi.org/10.65215/LTSpreprints.2026.04.18.000189. This version posted April 18, 2026. The copyright holder for this preprint (which was not certified by peer review) is the author/funder. Creative Commons license: CC Attribution-NonCommercial-NoDerivatives 4.0 https://creativecommons.org/licenses/by-nc-nd/4.0

mechanics/molecular mechanics simulations revealed no significant structural perturbations during catalysis, either globally or at interfacial residues. Over 100 ps simulations, the RMSD for all atoms or Cα atoms at the interfaces remained within 1.2–1.6 Å, while the RMSD of all protein Cα atoms stayed below 1.0 Å (Figure 5b, Supplementary Figure 9a–g). These data together rule out allosteric regulation mediated by assembly interfaces. Moreover, the catalytic sites remain accessible through Interface B in the assembly state (Figure 5c), and the hollow fibers organize into a porous lamellar architecture (Figure 3d). This configuration concentrates enzymes while preserving extensive surface accessibility, thereby maintaining efficient substrate entry and product diffusion. Collectively, these findings indicate that UOX assembly function neither as stress-induced storage forms nor as allosteric regulators, but instead represent a metabolically active state that sustains efficient urate turnover within peroxisomes.

To directly test the functional relevance of this organization *in vivo*, we engineered a UOX variant designed to selectively disrupt helix tiling assembly while preserving tetrameric organization and catalytic function. Guided by structural comparison with the non-assembling *Aspergillus flavus* homolog [49], we introduced steric hindrance at Interface C by replacing residues 200-206 with the corresponding loop sequence in *Aspergillus flavus* (Figure 5d, Supplementary Table 3). The resulting variant formed stable tetramer and retained normal catalytic activity (Supplementary Figure 10a-c, Supplementary Table 4). We then generated liver-specific *Uox* knockout mice and rescued hepatic expression with either wild-type or mutant UOX at endogenous levels (Supplementary Figure 10d-e). Electron microscopy confirmed the complete absence of high-order UOX assemblies in the mutant peroxisomes, without detectable alteration in overall peroxisomal morphology (Figure 5e-f, Supplementary Figure 10g-j). Despite the loss of UOX assembly formation, mutant mice exhibited serum urate concentrations indistinguishable from controls (Figure 5g). These findings demonstrate that UOX assembly formation is dispensable for maintaining urate homeostasis under baseline physiological conditions, suggesting that the tetrameric form alone is sufficient to

Langtaosha (LTS) Preprint doi: https://doi.org/10.65215/LTSpreprints.2026.04.18.000189. This version posted April 18, 2026. The copyright holder for this preprint (which was not certified by peer review) is the author/funder. Creative Commons license: CC Attribution-NonCommercial-NoDerivatives 4.0 https://creativecommons.org/licenses/by-nc-nd/4.0

sustain catalytic flux *in vivo*.

We therefore considered whether the primary advantage of assembly lies not in regulating catalysis but in enhancing molecular robustness through solid-state organization. Indeed, compared with tetrameric UOX, the assembled state showed an ~5 °C increase in melting temperature and markedly increased resistance to Proteinase K digestion (Fig. 5h–i). To probe protection from oxidative damage in a peroxisome-relevant context, we treated primary hepatocytes from rescue mice with 3-amino-1,2,4-triazole (3-AT) to induce peroxisomal oxidative stress and quantified oxidative modifications of UOX. UOX in the assembled state exhibited reduced oxidative modification, as assessed by both free cysteine analysis and mass spectrometry (Fig. 5j–k). Because oxidative modifications can compromise activity and promote degradation [50-52], these data support a functional model in which helix-tiling assembly stabilizes UOX against chemical and proteolytic stress, enabling sustained catalysis in the peroxide-rich peroxisomal matrix and contributing to long-term metabolic robustness.

Discussion

Our *in situ* cryo-electron tomography (cryo-ET) analysis reveals a previously unrecognized helix tiling assembly formed by urate oxidase (UOX) within mouse hepatic peroxisomes. By resolving this architecture directly in native tissue at molecular resolution, our study underscores the power of cryo-ET to uncover high-order intracellular organizations that are not readily accessible by *in vitro* reconstitution or conventional structural approaches. The detailed architecture of the UOX assembly shows that the high-order organization is mediated by weak, multivalent interactions between homotetramers involving several short structural motifs. This finding is consistent with previous work demonstrating that subtle sequence features can dramatically influence supramolecular assembly behavior [53-55]. Although no single residue appears indispensable for assembly formation, the interactions are sufficiently fragile that insertion of a short unstructured loop completely abolishes the high-order

Langtaosha (LTS) Preprint doi: https://doi.org/10.65215/LTSpreprints.2026.04.18.000189. This version posted April 18, 2026. The copyright holder for this preprint (which was not certified by peer review) is the author/funder. Creative Commons license: CC Attribution-NonCommercial-NoDerivatives 4.0 https://creativecommons.org/licenses/by-nc-nd/4.0

organization. This sensitivity complicates evolutionary inference from sequence alone, nevertheless, our comparative structural and phylogenetic analyses indicate that the assembly is conserved among UOX-expressing mammals but not across Chordata, suggesting that it may represent a lineage-specific evolutionarily advantageous adaptation.

Molecular assemblies arising from molecular crowding—driven by weak, often transient interactions—are pervasive in cells and frequently leads to phase separated condensates or high-order solid-like states[16]. Metabolic enzymes are particularly prone to such organization, and in many cases such assembly formation is coupled to allosteric regulation of catalytic activity, enabling rapid metabolic control beyond transcriptional regulation[56,57]. While the UOX assembly we described can be reconstituted *in vitro*, it forms only rarely under dilute conditions, indicating that the crowded peroxisomal matrix plays an active role in promoting assembly formation beyond intrinsic sequence determinants. Importantly, unlike many previously described enzyme assemblies, UOX polymerization does not measurably alter catalytic activity, arguing against a regulatory role and instead pointing to a distinct functional logic.

Structurally, the fivefold symmetry of UOX's hollow fiber architecture precludes space-filling crystal packing, instead yielding a porous lamellar organization that maximizes surface area while maintaining stability. This solid-state assembly is well suited to preserve substrate accessibility and product diffusion while conferring substantial protection against thermal, proteolytic, and oxidative stress. Such stabilization is likely advantageous in the peroxisomal environment, which is enriched in hydrogen peroxide—a reactive by-product of UOX catalysis. More broadly, our findings illustrate how high-order enzyme organization can evolve to optimize molecular stability in harsh intracellular environments without compromising catalytic efficiency, expanding current paradigms of metabolic enzyme organization in crowded intracellular environments.

Langtaosha (LTS) Preprint doi: https://doi.org/10.65215/LTSpreprints.2026.04.18.000189. This version posted April 18, 2026. The copyright holder for this preprint (which was not certified by peer review) is the author/funder. Creative Commons license: CC Attribution-NonCommercial-NoDerivatives 4.0 https://creativecommons.org/licenses/by-nc-nd/4.0

UOX catalyzes urate oxidation to 5-hydroxyisourate, which *in vivo* is further processed by HIU hydrolase and OHCU decarboxylase into S-(+)-allantoin [58,59]. In certain microorganisms, these enzymes assemble into multienzyme complexes [60], raising the possibility that peroxisomal UOX assemblies may similarly coordinate downstream partners. Although our subtomogram averages do not reveal stable, high-occupancy association of these enzymes with the UOX assembly, transient or low-stoichiometry interactions cannot be excluded and warrant further investigation.

UOX was lost during hominoid evolution, resulting in urate becoming the terminal product of human purine catabolism—a change with important physiological and pathological consequences, including susceptibility to hyperuricemia and gout. Current treatments for hyperuricemia include urate synthesis inhibitors, uricosuric agents, and uricolytic enzymes [61]. The later, such as recombinant *Aspergillus flavus* uricase Rasburicase (ELITEKR) [62] and the porcine–baboon chimeric enzyme Pegloticase (KRYSTEXXA) [63], are effective but limited by their short plasma half-life and immunogenicity [64]. Although substantial effort has focused on engineering improved UOX variants [65,66], our identification of a native higher-order UOX assembly suggests that intrinsic self-association could influence therapeutic enzyme behavior *in vivo*. For example, if administered UOX were to self-associate under physiological conditions, this could alter effective particle size, diffusion and local microenvironment, with potential consequences for stability, distribution and activity. These considerations motivate strategies to control oligomeric state and formulation—such as tuning surface interfaces or using encapsulation approaches [67-69]—to preserve stability while minimizing unintended aggregation.

Acknowledgments

We thank Prof. Ning Gao, and Prof. Junyu Xiao for the critical suggestions. We are grateful to the Cryo-EM Platform of Peking University and Changping Laboratory for data collection, the High-Performance Computing Platform of Peking University for assistance with computation, and the National Centre for Protein Sciences at Peking

Langtaosha (LTS) Preprint doi: https://doi.org/10.65215/LTSpreprints.2026.04.18.000189. This version posted April 18, 2026. The copyright holder for this preprint (which was not certified by peer review) is the author/funder. Creative Commons license: CC Attribution-NonCommercial-NoDerivatives 4.0 https://creativecommons.org/licenses/by-nc-nd/4.0

University for technical assistance. We thank Dr. Ying-Chun Hu, Zhen-Yang Kong and Meng-ting Xing for their technical assistance in EM sample preparation and image analysis at the Core Facilities of School of Life Sciences, Peking University. This work is funded by the National Key Research and Development Program of China (#2024YFA1802800 to Q.G.), the National Natural Science Foundation of China (#32371191 to Q.G.) and the Beijing Natural Science Foundation (JQ24031 to Q.G.). Additional funds to Q.G. are provided by the Center for Life Sciences at Peking University. Q.G. is supported by Changping Laboratory. The authors declare no competing financial interests.

Data availability

The representative tomogram from mouse liver has been deposited in the Electron Microscopy Data Bank (EMDB) under the accession code EMD-68842. The subtomogram averaging maps have been deposited in the EMDB under the accession codes EMD-68843 and EMD-68844 for mouse UOX assembly; EMD-68845 and EMD-68846 for porcine UOX assembly; EMD-68847 and EMD-68848 for rat UOX assembly. Cryo-EM coordinates and density maps have been deposited in the Protein Data Bank (PDB) and EMDB under the accession codes PDB 23BS (EMD-68839) for mouse UOX in the apo state; PDB 23BT (EMD-68840) for mouse UOX complexed with UA; PDB 23BU (EMD-68841) for mouse UOX assembly isolated from liver.

Author information

These authors contributed equally: Junhan Yang, Zhe Chen, Yonglun Wang.

Contributions

Q.G. and X.C. conceived and designed the experiments. J.Y., W.D., Z.Y. and Y.Z. prepared samples for the cryo-ET study. J.Y., W.D. and Z.Y. collected the cryo-ET data. J.Y., W.D., Z.Y., Z.L. and S.L. processed the data and performed subtomogram averaging. J.Y., Z.C. and Z.Y. prepared samples, collected and processed data for the cryo-EM study. J.Y. and Z.C. built and refined the models. J.Y. and Z.C. designed and

Langtaosha (LTS) Preprint doi: https://doi.org/10.65215/LTSpreprints.2026.04.18.000189. This version posted April 18, 2026. The copyright holder for this preprint (which was not certified by peer review) is the author/funder. Creative Commons license: CC Attribution-NonCommercial-NoDerivatives 4.0 https://creativecommons.org/licenses/by-nc-nd/4.0

performed the mutant protein assays. J.Y., Z.Y. and Z.C. performed enzyme activity assays. S.Y. performed the MD analysis. X.S. and C.K. performed the sequence alignment and phylogenetic analysis. Y.W. prepared the mice and primary hepatocytes, performed serum uric acid and free cystines detection assays. X.S. performed the mass spectrometry assays. J.Y., Z.C., Y.W., S.Y., X.S. and C.K. prepared the figures. J.Y., Z.C., Z.Y., Y.W., S.Y., X.S., C.K. and X.S. analyzed and interpreted the results. Q.G. wrote the paper with the help of J.Y., Z.C., Y.W., S.Y., X.S. and C.K., and all authors reviewed and revised it.

Corresponding authors:

Correspondence to Xiaowei Chen, Qiang Guo

Ethics declarations

Competing interests

The authors declare no competing interests.

Langtaosha (LTS) Preprint doi: https://doi.org/10.65215/LTSpreprints.2026.04.18.000189. This version posted April 18, 2026. The copyright holder for this preprint (which was not certified by peer review) is the author/funder. Creative Commons license: CC Attribution-NonCommercial-NoDerivatives 4.0 https://creativecommons.org/licenses/by-nc-nd/4.0

Figure legends

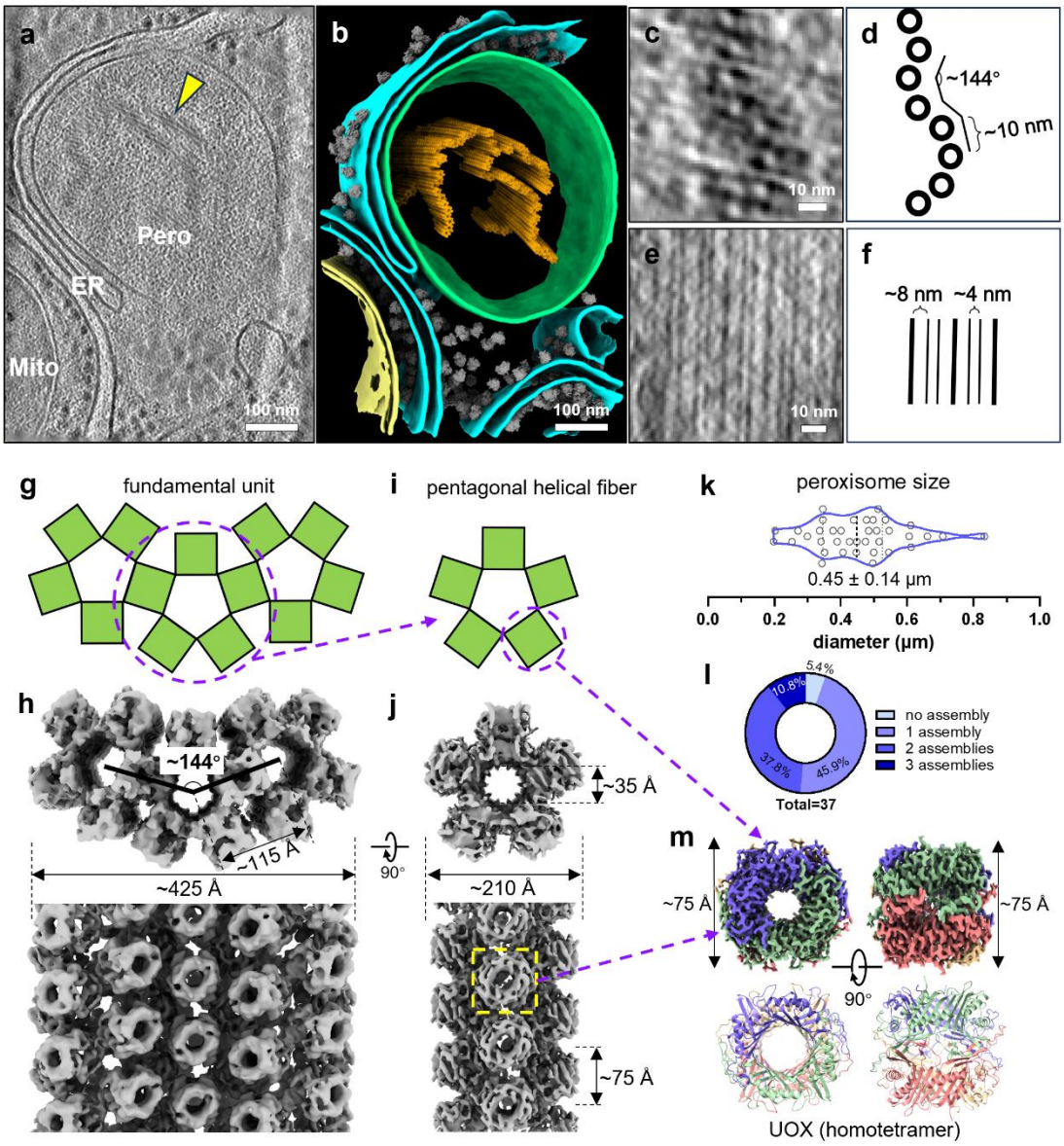

Figure 1: A supramolecular urate oxidase assembly in mouse hepatic peroxisomes

a, 1.1 nm thick tomographic slice of a representative tomogram acquired from high-pressure-frozen mouse livers. The yellow arrowhead indicates a supramolecular UOX assembly within a peroxisome. Pero, peroxisome. Mito, mitochondrion. Scale bars, 100 nm.

b, Three-dimensional rendering of the segmentation from the tomogram shown in (**a**). Yellow, mitochondrion. Magenta, ER membrane. Grey, ribosome. Green, peroxisome. Orange, the UOX assembly. Scale bars, 100 nm.

c-d, Representative top view (**c**) and corresponding schematic (**d**) of the UOX assembly.

Langtaosha (LTS) Preprint doi: https://doi.org/10.65215/LTSpreprints.2026.04.18.000189. This version posted April 18, 2026. The copyright holder for this preprint (which was not certified by peer review) is the author/funder. Creative Commons license: CC Attribution-NonCommercial-NoDerivatives 4.0 https://creativecommons.org/licenses/by-nc-nd/4.0

Scale bars, 10 nm.

e-f, Representative side view (**e**) and corresponding schematic (**f**) of the UOX assembly. Scale bars, 10 nm.

g-h, The schematic representation (**g**) and subtomogram averaging map (**h**) of the fundamental repeating unit of the UOX assembly.

i-j, The schematic representation (**i**) and subtomogram averaging map (**j**) of a single helical fiber within the UOX assembly.

k, Violin plot showing peroxisome diameter distribution measured from tomograms. Data are presented as mean ± SD.

l, Proportion of peroxisomes containing different numbers of UOX assemblies.

m, Single-particle cryo-EM density map (top) and atomic model (bottom) of mouse urate oxidase.

Langtaosha (LTS) Preprint doi: https://doi.org/10.65215/LTSpreprints.2026.04.18.000189. This version posted April 18, 2026. The copyright holder for this preprint (which was not certified by peer review) is the author/funder. Creative Commons license: CC Attribution-NonCommercial-NoDerivatives 4.0 https://creativecommons.org/licenses/by-nc-nd/4.0

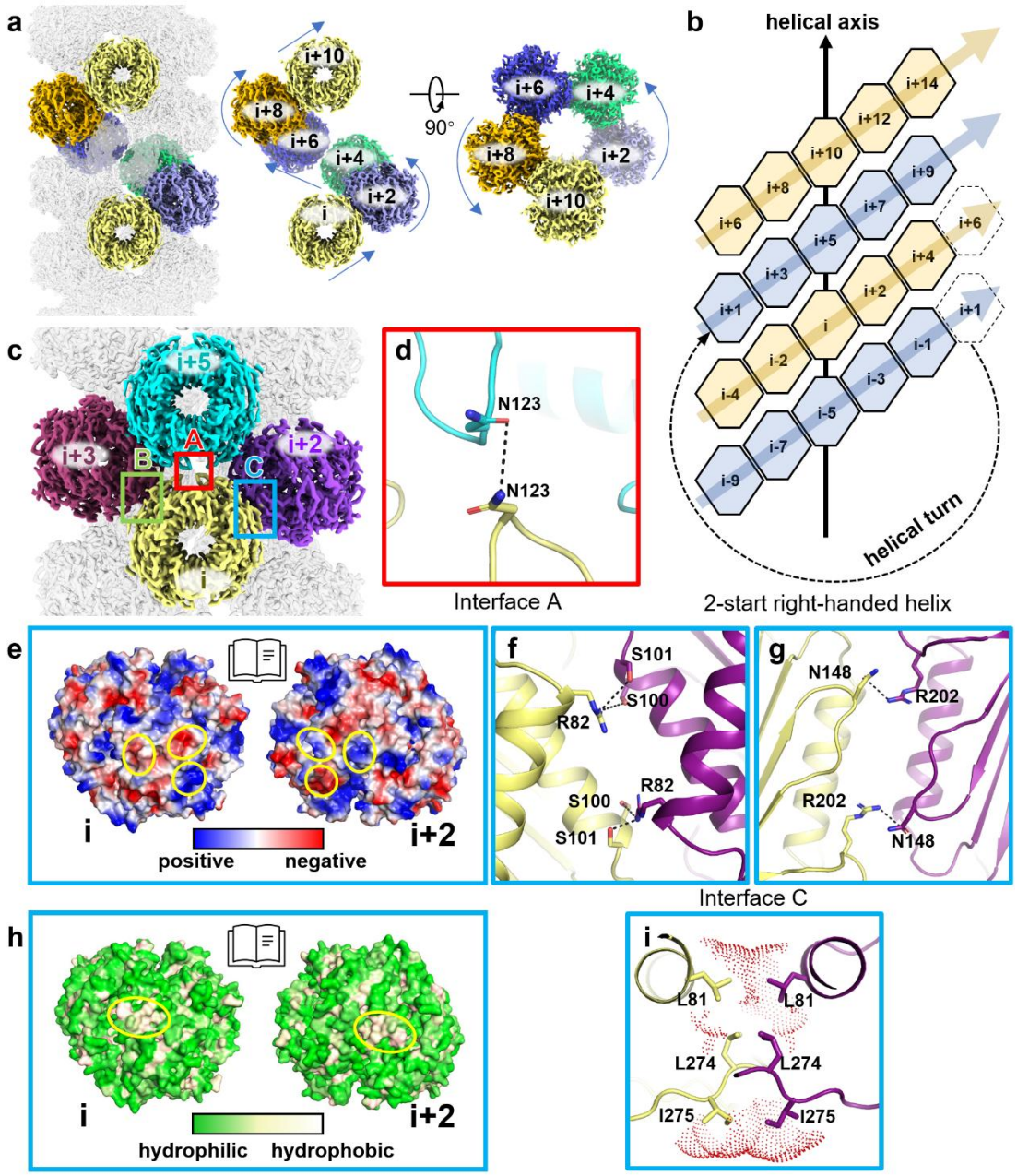

Figure 2: Inter-tetramer interactions governing UOX helical fiber

a, Left, an individual helix from the UOX assembly. Middle and right, the side view and top view of the individual helix, with homotetrameric subunits labeled by index number; blue arrows showing the helix extension direction.

b, Two-dimensional schematic of the UOX helical fiber. Each homotetrameric subunit is assigned a unique index number. The yellow and purple colors represent the two strands of the double helix. Arrows indicate the direction of helix extension.

c, Localization of inter-subunit interfaces within the UOX helical fiber. Interface A,

Langtaosha (LTS) Preprint doi: https://doi.org/10.65215/LTSpreprints.2026.04.18.000189. This version posted April 18, 2026. The copyright holder for this preprint (which was not certified by peer review) is the author/funder. Creative Commons license: CC Attribution-NonCommercial-NoDerivatives 4.0 https://creativecommons.org/licenses/by-nc-nd/4.0

Interface B and Interface C are highlighted by red, green and blue boxes, respectively.

d, Key residues involved in the formation of interface A.

e, Open-book view of the electrostatic surface potential at Interface C between UOX homotetramers i and i+2. Blue and red indicate positive and negative charge, respectively. Yellow circles mark specific interaction regions.

f-g, Key residues corresponding to regions marked in (**e**) that contribute to the formation of interface C.

h, Open-book view of hydrophobic surface properties at Interface C between UOX homotetramers i and i+2. Green indicates hydrophilic regions, and white indicates hydrophobic regions. Yellow circle highlight interaction sites.

i, Key residues corresponding to regions marked in (**h**) that contribute to the formation of interface C.

Langtaosha (LTS) Preprint doi: https://doi.org/10.65215/LTSpreprints.2026.04.18.000189. This version posted April 18, 2026. The copyright holder for this preprint (which was not certified by peer review) is the author/funder. Creative Commons license: CC Attribution-NonCommercial-NoDerivatives 4.0 https://creativecommons.org/licenses/by-nc-nd/4.0

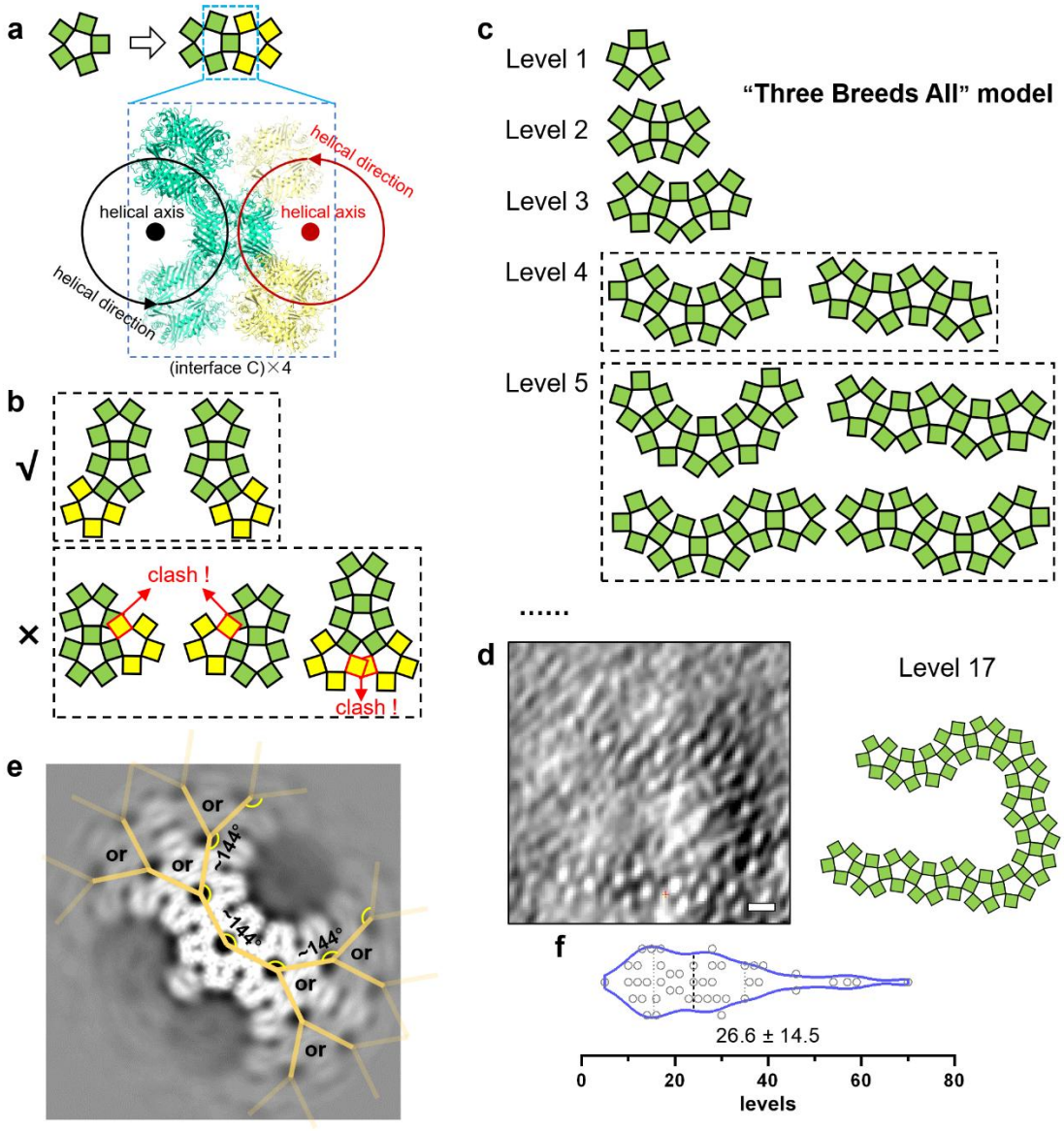

Figure 3: Lateral propagation rules and lamellar architecture of the UOX helix tiling assembly

a, Schematic model of lateral extension of UOX helical fibers through sharing a column of homotetramers via four interface C interactions. Green squares denote homotetramers in the original fiber; yellow squares indicate newly incorporated homotetramers. The helical axis and direction are indicated by dots and arrowed circles, respectively.

b, (Top) Schematic illustrating permitted lateral extension involving three adjacent fibers. (Bottom) Schematic of a sterically prohibited configuration resulting from simultaneous extension into two immediately neighboring directions. Sterically clashed

Langtaosha (LTS) Preprint doi: https://doi.org/10.65215/LTSpreprints.2026.04.18.000189. This version posted April 18, 2026. The copyright holder for this preprint (which was not certified by peer review) is the author/funder. Creative Commons license: CC Attribution-NonCommercial-NoDerivatives 4.0 https://creativecommons.org/licenses/by-nc-nd/4.0

subunits are highlighted with red boxes.

c, The “Three Breeds All” describing hierarchical lateral propagation of UOX fibers, in which a three adjacent fibers unit serves as the repeating module for lamellar growth. The number of fibers is indicated by level annotations.

d, Representative lateral extension pattern observed in a tomogram (left) and its corresponding schematic (right). Scale bars, 10 nm.

e, Z-axis projection of the subtomogram averaging density map of a fundamental unit, revealing a tree-like extension pattern. Yellow lines indicate potential extension paths.

f, Violin plot showing the distribution of extension levels per assembly. Data are presented as mean ± SD.

Langtaosha (LTS) Preprint doi: https://doi.org/10.65215/LTSpreprints.2026.04.18.000189. This version posted April 18, 2026. The copyright holder for this preprint (which was not certified by peer review) is the author/funder. Creative Commons license: CC Attribution-NonCommercial-NoDerivatives 4.0 https://creativecommons.org/licenses/by-nc-nd/4.0

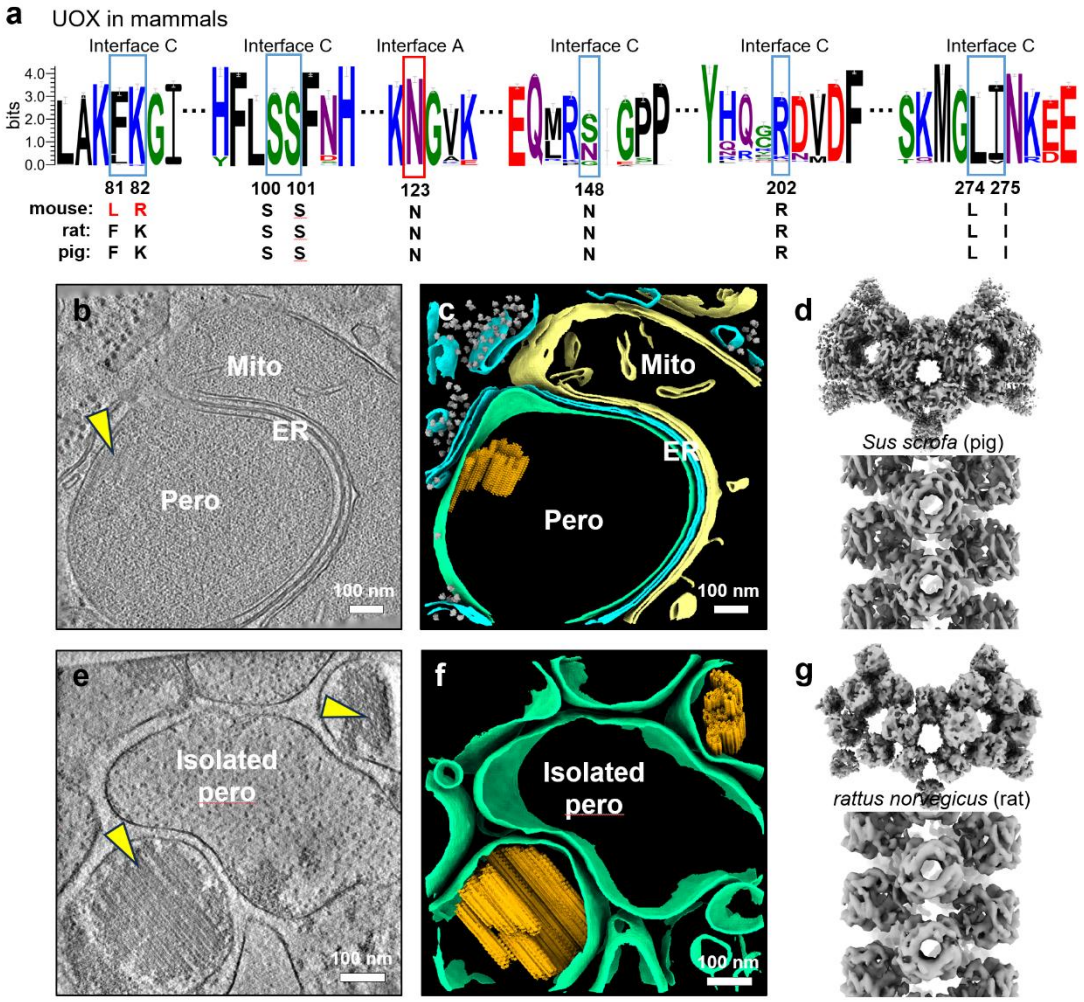

Figure 4: Conservation of the UOX helix tiling assembly across mammals.

a, Sequence conservation analysis of specific UOX motifs in Mammalia (n = 313), generated with WebLogo3 [70]. Residues directly involved in interactions are boxed in red (Interface A) or blue (Interface C), with those from mouse, rat and pig listed below. Numbers indicate corresponding residue positions in mouse UOX (UniProt ID: P25688).

b, 1.4 nm thick tomographic slice of a representative tomogram collected from high-pressure frozen porcine liver. Yellow arrowhead indicates UOX assembly. Pero, peroxisome. Mito, mitochondrion. Scale bars, 100 nm.

c, Three-dimensional rendering of the segmentation from the tomogram shown in (**b**). Yellow, mitochondrion. Magenta, ER membrane. Grey, ribosome. Green, peroxisome. Orange, the UOX assembly. Scale bars, 100 nm.

d, (Top) Subtomogram averaging density map of the fundamental unit of porcine UOX

Langtaosha (LTS) Preprint doi: https://doi.org/10.65215/LTSpreprints.2026.04.18.000189. This version posted April 18, 2026. The copyright holder for this preprint (which was not certified by peer review) is the author/funder. Creative Commons license: CC Attribution-NonCommercial-NoDerivatives 4.0 https://creativecommons.org/licenses/by-nc-nd/4.0

524 assembly. (Bottom) Side view of a single UOX helical fiber within the assembly.
525 **e**, 1.2 nm thick tomographic slice of a representative tomogram collected from hepatic
526 peroxisomes isolated from rat liver. Yellow arrowhead indicates UOX assembly. Pero,
527 peroxisome. Scale bars, 100 nm.
528 **f**, Three-dimensional rendering of the segmentation from the tomogram shown in (**e**).
529 Green, peroxisome. Orange, the UOX assembly. Scale bars, 100 nm.
530 **g**, (Top) Subtomogram averaging density map of the fundamental unit of rat UOX
531 assembly. (Bottom) Side view of a single UOX helical fiber within the assembly.
532
533

Langtaosha (LTS) Preprint doi: https://doi.org/10.65215/LTSpreprints.2026.04.18.000189. This version posted April 18, 2026. The copyright holder for this preprint (which was not certified by peer review) is the author/funder. Creative Commons license: CC Attribution-NonCommercial-NoDerivatives 4.0 https://creativecommons.org/licenses/by-nc-nd/4.0

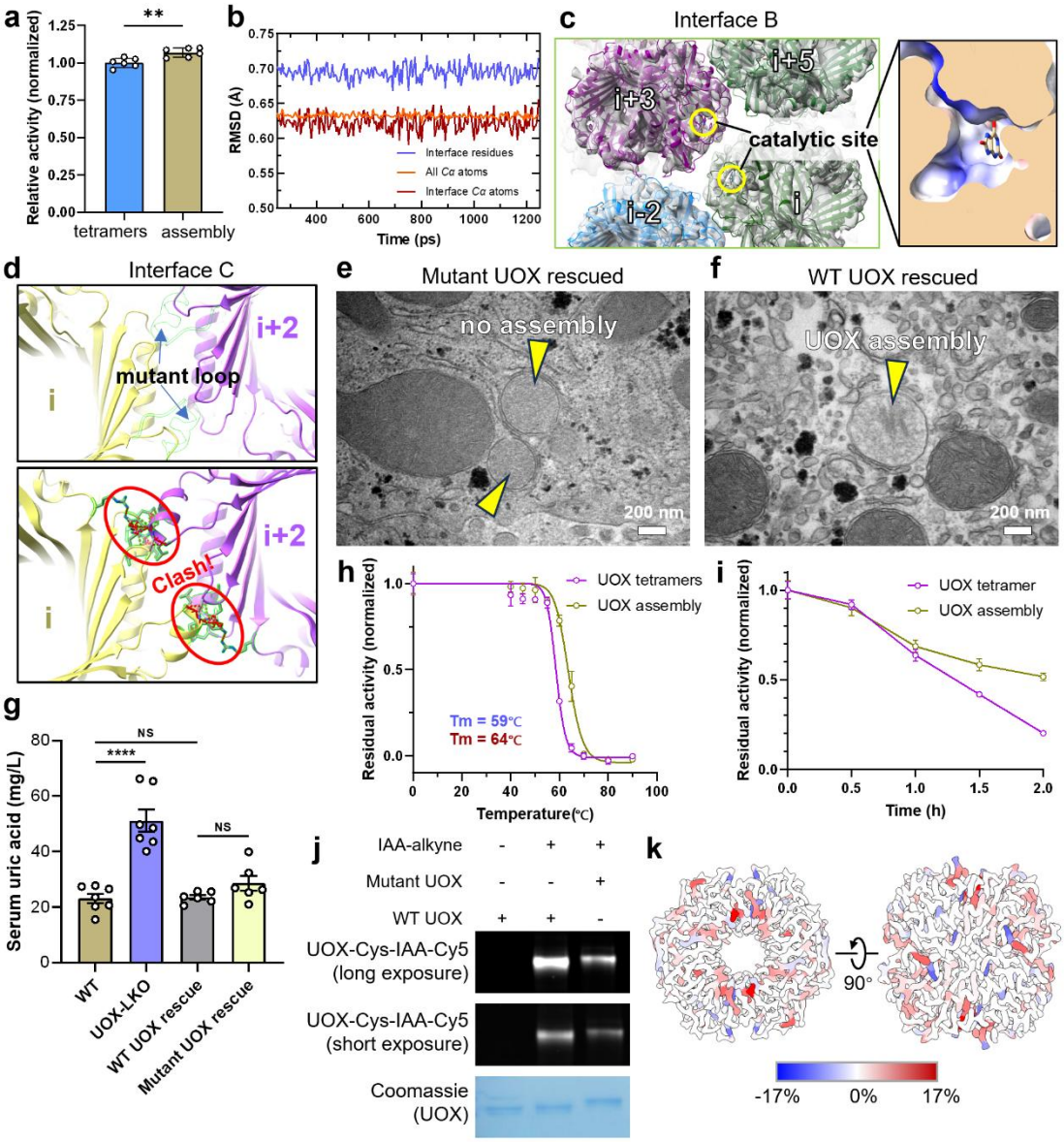

Figure 5: Functional consequences of UOX assembly formation.

a, Relative enzyme activity of UOX tetramers and assembly. UOX abundance was assessed by western blot. Relative activity is normalized to the mean activity of the tetramer form. Data are presented as mean ± SD; individual data points are shown. Statistical significance was assessed by Welch's unpaired *t*-test; $P<0.05$ was considered significant.

b, Root-mean-square deviation (RMSD) plot of UOX in complex with substrate during the equilibration phase of the molecular dynamic simulation, with the UOX structure determined in this research used as the reference.

c, Structural details of interface B in the UOX assembly, showing that all active sites

Langtaosha (LTS) Preprint doi: https://doi.org/10.65215/LTSpreprints.2026.04.18.000189. This version posted April 18, 2026. The copyright holder for this preprint (which was not certified by peer review) is the author/funder. Creative Commons license: CC Attribution-NonCommercial-NoDerivatives 4.0 https://creativecommons.org/licenses/by-nc-nd/4.0

remain accessible. Yellow circles indicate active sites; UOX homotetramers are labeled by index number.

d, Structural basis for selective disruption of UOX assembly. The mutant UOX is fitted to the assembly density map and aligned with wild-type UOX, revealing steric hindrance introduced by replacement of residues 200–206 with the corresponding loop sequence from *Aspergillus flavus* at interface C. (Top) The substituted loop is highlighted. (Bottom) Predicted steric clashes are marked with red dotted lines.

e, Representative transmission electron micrograph of liver from wild-type UOX rescue mice. Yellow arrowheads indicate peroxisomes containing typical UOX assembly. Scale bars, 200 nm.

f, Representative transmission electron micrograph of liver from mutant UOX rescue mice. Yellow arrowheads indicate peroxisomes lacking UOX assembly. Scale bars, 200 nm.

g, Serum uric acid level of wild-type, *Uox* liver specific knockout (LKO), WT UOX rescue and mutant UOX rescue mice. The data are presented as the mean ± SD, with each data point reflecting one mouse. Statistical significance was analyzed using unpaired t -test, with $P < 0.05$ considered statistically significant.

h, Thermostability of UOX tetramers and assembly, assessed by residual activity after incubation at indicated temperatures. The temperatures at which the enzymes retained half of their activity (Tm) were determined in GraphPad Prism 9. The data are presented as the mean ± SD.

i, Proteinase K resistance of UOX tetramers and assembly, plotted as residual activity after digestion for the indicated times. The data are presented as the mean ± SD.

j, Functional cysteine levels of UOX (WT and assembly-disrupting mutant) purified from primary hepatocytes, which were isolated from rescue mouse livers and cultured with 10 mM 3-AT. UOX protein levels were quantified by Coomassie Blue staining.

k, Mass spectrometry analysis of oxidative modifications on UOX purified from primary hepatocytes isolated from mouse livers and cultured in presence of 10 mM 3-AT. Red indicates residues exhibiting higher levels of oxidative modification in the assembly-disrupting mutant relative to wild-type UOX, whereas blue indicates lower

Langtaosha (LTS) Preprint doi: https://doi.org/10.65215/LTSpreprints.2026.04.18.000189. This version posted April 18, 2026. The copyright holder for this preprint (which was not certified by peer review) is the author/funder. Creative Commons license: CC Attribution-NonCommercial-NoDerivatives 4.0 https://creativecommons.org/licenses/by-nc-nd/4.0

575 modification levels.

576

Langtaosha (LTS) Preprint doi: https://doi.org/10.65215/LTSpreprints.2026.04.18.000189. This version posted April 18, 2026. The copyright holder for this preprint (which was not certified by peer review) is the author/funder. Creative Commons license: CC Attribution-NonCommercial-NoDerivatives 4.0 https://creativecommons.org/licenses/by-nc-nd/4.0

Methods

High-pressure freezing

The mouse liver samples were vitrified using a previous established protocol [14,71] with some modifications. In brief, the abdomen of each mouse was dissected under anesthesia. A small piece of liver tissue was meticulously excised using a scalpel and immersed in phosphate-buffered saline (PBS) supplemented with 20% (w/v) dextran and 5% (w/v) sucrose for 30 s before being placed onto an EM grid (copper, 200 mesh, Beijing XXBR., Catalogue no. T10012). The grid was coated with an additional carbon layer (~20 nm thick) and freshly glow discharged using a Model 950 Advanced Plasma System (Gatan, Pleasanton, CA, USA) before usage. The grid was previously placed into a 6 mm aluminum carrier (200 nm in depth). After filling the carrier with 2-methylpentane (Sigma), a 6 mm sapphire disc was immediately placed on top of the carrier. The assembly of the sandwich carrier was promptly inserted into the high-pressure cryostat (Leica EM ICE) for vitrification. The vitrified sandwich assembly was then transferred to a liquid ethane and propane mixture (ethane:propane=36.9%:63.1%) at -170°C, allowing 2-methylpentane to dissolve. The resulting grid was then transferred to liquid nitrogen for storage until milling.

For porcine liver samples, fresh livers were obtained from a local market and processed immediately. Tissue samples were separated using a sterile biopsy punch and immersed in phosphate-buffered saline (PBS) supplemented with 20% (w/v) dextran and 5% (w/v) sucrose for 30 s. Samples were then transferred onto an EM grid same as above. Subsequent procedures were performed under identical parameters as described for mouse liver tissues.

The cryo-lift-out and lamella thinning

A cryo-FIB (Aquilos 2, Thermo Fisher Scientific) was employed to prepare lamellae, using an adapted serial lift-out method [71,72]. Briefly, the grid was clipped into an Autogrid (ThermoFisher Scientific) before being loaded onto the FIB chamber via the sample transfer rod. To minimize the ion beam damage and enhance the electrical

Langtaosha (LTS) Preprint doi: https://doi.org/10.65215/LTSpreprints.2026.04.18.000189. This version posted April 18, 2026. The copyright holder for this preprint (which was not certified by peer review) is the author/funder. Creative Commons license: CC Attribution-NonCommercial-NoDerivatives 4.0 https://creativecommons.org/licenses/by-nc-nd/4.0

conductivity, the sample was coated with a layer of platinum (Pt) using gas injection system (GIS) for 2 min, followed by sputtering at 30 mA for 15 s. Initially, a copper block (~10×15 μm) is milled from the half-grid (copper, Beijing XXBR., Catalogue no. T1109M-3) at room temperature and attached to the Easylift needle by redeposition (beam current: 1 nA). Next, four trenches were milled around the region of interest with the ion beam (beam current: 3 nA) to expose the sample block. This block was subsequently attached to the copper block by redeposition (beam current: 0.5 nA) and transferred to the receiver grid (copper, 100/400 mesh, Beijing XXBR., Catalogue no. G100/400), where it was serially sectioned to several lamellae with a thickness of ~3 μm. These lamellae were securely attached to the grid in turn by two-sided redeposition method (beam current: 0.5 nA). Finally, each lamella was finely milled (beam current from 1 nA to 30 pA) to a target thickness of approximal 200 nm, which was then used for subsequent tomographic data acquisition.

Cryo-ET Data Acquisition

For lamellae from mouse livers, they were loaded to a 300 kV cryo-transmission electron microscope Titan Krios G3 (ThermoFisher Scientific) equipped with a K3 camera and a Gatan energy filter. Automatic tomographic tilt series acquisition was performed using SerialEM software [73] with the Plugin PACE-tomo [74]. Images were acquired at a magnification of 64000× (pixel size was 1.37 Å) in TIFF format using super-resolution mode, resulting in 10 frames per image. The defocus was set from -4.0 to -6.0 μm. The acquisition was performed from -50° to +50° (with respect to the pre-tilt angle) in 2° increments, utilizing the dose symmetric scheme [75,76]. The dose rate was set to 13 e/pixel/s and total dose was limited to 120 e/Å^2 per tilt series.

For lamellae from porcine livers, they were loaded to a 300 kV cryo-transmission electron microscope Titan Krios G4 (ThermoFisher Scientific) with a Falcon 4 camera and a ThermoFisher Selectris X energy filter. Automatic tomographic tilt series acquisition was performed using Tomography 5.12.0 (ThermoFisher Scientific). Images were acquired at a magnification of 53000× (pixel size was 2.37 Å) in EER

Langtaosha (LTS) Preprint doi: https://doi.org/10.65215/LTSpreprints.2026.04.18.000189. This version posted April 18, 2026. The copyright holder for this preprint (which was not certified by peer review) is the author/funder. Creative Commons license: CC Attribution-NonCommercial-NoDerivatives 4.0 https://creativecommons.org/licenses/by-nc-nd/4.0

format. The defocus was set from -4.0 to -6.0 μm. The acquisition was performed from -44° to +44° (with respect to the pre-tilt angle) in 2° increments, utilizing the dose symmetric scheme. The dose rate was set to 9.74 e/pixel/s and total electron dose per tilt series was limited to 120 e/Å^2.

For isolated peroxisomes from rat livers, they were loaded to a 300 kV cryo-transmission electron microscope Titan Krios G4 (ThermoFisher Scientific) with a Falcon 4 camera and a ThermoFisher Selectris X energy filter. Automatic tomographic tilt series acquisition was performed using Tomography 5.12.0 (ThermoFisher Scientific). Images were acquired at a magnification of 64000× (pixel size was 1.94 Å) in EER format. The defocus was set from -3.0 to -5.0 μm. The acquisition was performed from -50° to +50° in 2° increments, utilizing the dose symmetric scheme. The dose rate was set to 7.87 e/pixel/s and total electron dose per tilt series was limited to 120 e/Å^2.

Tomogram reconstruction and denoising

TOMOMAN [77] and TOM toolbox [78] were used as general tools in image processing. Initially, for TIFF format files, all frames of each tilt were motion corrected using MotionCor2 software [79]. While for EER format files, the frames with a dose of approximal 0.10 e/Å^2 were fractioned (depend on the specific EER frames) before motion correction by MotionCor2 software. After cleaning bad tilts and dose filtering[80], each tilt series was aligned using patch-tracking method either in AreTomo2 software[81] or in IMOD software [82], followed by reconstructing using back projection method to obtain a tomogram. All tomograms were rescaled before further processing. Specifically, the tomograms from mouse livers were binned by a factor of 8, while tomograms from porcine livers and rat peroxisomes used a binning factor of 6 depending on the specific pixel size. For visualization, tomograms were denoised either with cryoCARE [83] or IsoNet [84] before a deconvolution filter were applied to further improve the contrast [85].

Langtaosha (LTS) Preprint doi: https://doi.org/10.65215/LTSpreprints.2026.04.18.000189. This version posted April 18, 2026. The copyright holder for this preprint (which was not certified by peer review) is the author/funder. Creative Commons license: CC Attribution-NonCommercial-NoDerivatives 4.0 https://creativecommons.org/licenses/by-nc-nd/4.0

667 **Subtomogram averaging**

668 Subtomogram averaging was performed using an integrated workflow involving
669 software: IMOD [82], Warp [85], RELION [86], M [87], and ChimeraX [88].
670
671 Mouse UOX assembly were manually traced as fibers in IMOD, with at least three
672 points per fiber marked to define their trajectories. Coordinates were saved in .mod
673 format and converted to text files using the "model2point" command in IMOD. Custom
674 scripts were used to split these text files into individual fiber-specific coordinate lists.
675 Fiber coordinates were oversampled at 70 Å intervals using the "relion_helix_toolbox"
676 command, generating 25,040 points in total. Subtomograms (binning factor 4, box size
677 526 Å) were extracted based on these coordinates. Initial alignment was performed in
678 RELION/2.1 [89] via 3D auto-refinement, using the additional arguments "sigma_tilt=15"
679 and "sigma_psi=15". The initial reference map was directly 3D-reconstructed from the
680 subtomograms. Following alignment, the one representative fiber was re-centered
681 within the box and re-extracted. Another 3D auto-refinement in RELION/3.1 [90] yielded
682 an average map with three adjacent fibers. Manual adjustment of particle coordinates
683 and Euler angles was performed in ChimeraX using the ArtiaX plugin [91]. For
684 subtomograms derived from the same fiber, the coordinates should distribute evenly
685 (the distance = refined inter-segment distance) along the fiber axis; the Euler angle
686 orientations were the same and determined by the relative spatial positioning of two
687 adjacent fibers. The badly aligned particles were removed during manual adjustment.
688 Subtomograms were then re-extracted at the binning factor of 2 and locally refined with
689 tighter constraints on Euler angles before applying helical symmetry (rise=14.69 Å,
690 twist=-143.82°). The parameters were measured manually from the density map and
691 optimized using the "relion_helix_toolbox" command within a certain range. After
692 confirming helical symmetry, subtomograms were re-extracted at the binning factor of
693 2, retaining only the first 25 low-dose tilts from each tomogram to improve resolution.
694 Another round of 3D auto-refinement with helical symmetry and masking in
695 RELION/3.1 was conducted, followed by further optimization in M software through
696 improving tomogram alignment. The final refinement was processed in RELION/3.1

Langtaosha (LTS) Preprint doi: https://doi.org/10.65215/LTSpreprints.2026.04.18.000189. This version posted April 18, 2026. The copyright holder for this preprint (which was not certified by peer review) is the author/funder. Creative Commons license: CC Attribution-NonCommercial-NoDerivatives 4.0 https://creativecommons.org/licenses/by-nc-nd/4.0

with helical symmetry and masking [92], yielding a map at 7.3 Å resolution (final refined helical parameters: rise=14.53 Å, twist=-144.11°) with 17,221 subtomograms from 22 tomograms. The local resolution was estimated using Relion.

For subtomogram averaging of ribosomes, initial ribosome positions and orientations were determined by template matching using PyTOM [93] on five 8× binned tomograms, followed by manually screening. The results were fed to DeepFinder [94] to train a neural network for picking ribosomes on all remaining 8× binned tomograms, obtaining ~12,000 particles. After extracting subtomograms at 5.48 Å/px (4× binning) in Warp, they were subjected to iterative rounds of alignment and classification in RELION/3.1. The best class of ribosomes were 3D auto-refined before re-extracting at 2.74 Å/px (2× binning), followed by local 3D auto-refinement. The result was imported to M for improving alignment of tomograms before re-extracting at 2.055 Å/px (1.5× binning), followed by one more local 3D auto-refinement in RELION/3.1 and yielding a map at 9.6 Å resolution with 8,350 particles.

Membrane Segmentation and tomographic back-plotting

Tomograms were denoised and missing-wedge corrected by IsoNet prior to membrane segmentation, which was firstly performed using MemBrain-Seg [95] with the pre-trained model and then manually polished with Amira 3D 2022.2 (Thermo Fisher Scientific). Ribosomes and UOX assembly are the back-plotting of STA maps at coordinates after 3D refinement. A gaussian filter was applied to membranes and particles in ChimeraX for the final rendering.

Measurement of peroxisome size

The size of peroxisomes was estimated from tomograms. For each peroxisome, its size was determined by measuring the long-axis diameter of its largest cross-sectional slice within the tomogram.

Molecular cloning and mutagenesis

Langtaosha (LTS) Preprint doi: https://doi.org/10.65215/LTSpreprints.2026.04.18.000189. This version posted April 18, 2026. The copyright holder for this preprint (which was not certified by peer review) is the author/funder. Creative Commons license: CC Attribution-NonCommercial-NoDerivatives 4.0 https://creativecommons.org/licenses/by-nc-nd/4.0

The mouse urate oxidase gene (*mUox*, UniProt ID: P25688) was codon-optimized, synthesized and cloned into the pET-28a expression vector. The UOX bear an His-SUMO fusion tag at its N-terminal to facilitate the purification. Site-directed mutagenesis targeting the loop region spanning amino acid residues 200-206 was performed using Phanta Max Super-Fidelity DNA polymerase (Vazyme Biotech Co., Ltd), with mutated sequence on the primers. This mutagenesis enabled the replacement of the loop sequence with its homologous sequence from *Aspergillus flavus*. The resultant UOX mutant was validated through DNA sequencing prior to use.

Protein expression and purification

For the purification of His-SUMO-UOX (WT) and His-SUMO-UOX (mutant), the plasmids were transformed into BL21 (DE3) *E. coli* for protein expression. The transformed cells were grown at 37°C to OD_{600} 0.6–0.8. The culture was then cooled to 18°C and protein expression was induced by the addition of 0.5 mM IPTG for 18 h. Cells were harvested by centrifugation, the pellet was resuspended in lysis buffer (20 mM Tris, 150 mM NaCl, pH 8.0) before sonication and centrifugation. The supernatant was loaded onto a Ni-NTA agarose column for three times, washed with lysis buffer supplemented with 100 mM imidazole, and eluted with lysis buffer supplemented with 300 mM imidazole. The eluted fractions were concentrated to 1 mL before being loaded on a Superdex 200 Increase 10/300 GL (GE healthcare) column equilibrated with buffer B (100 mM $NaHCO_3$-Na_2CO_3, pH 10.4). The purity was confirmed by SDS-PAGE, and the protein was concentrated to at least 10 mg/mL for the replacement with lysis buffer before plunge freezing and stock at -80°C.

Isolation of peroxisomes from murine livers

The procedure for peroxisome isolation from murine livers was similar to the previously established protocol [96,97] by Andreas Manner et al. with some modifications. Briefly, following overnight starvation, approximately 10 g of murine liver tissue was excised. Tissues were rinsed three times with ice-cold phosphate-buffered saline (PBS) and homogenized in ice-cold HB buffer (250 mM sucrose, 5 mM MOPS, 1 mM EDTA,

Langtaosha (LTS) Preprint doi: https://doi.org/10.65215/LTSpreprints.2026.04.18.000189. This version posted April 18, 2026. The copyright holder for this preprint (which was not certified by peer review) is the author/funder. Creative Commons license: CC Attribution-NonCommercial-NoDerivatives 4.0 https://creativecommons.org/licenses/by-nc-nd/4.0

2 mM PMSF, 1 mM DTT, pH 7.4) using three homogenization cycles at 500 rpm on ice. The homogenate was centrifuged at 600 g for 10 min at 4°C to pellet debris, and the supernatant was retained. The pellet was re-homogenized under identical conditions and re-centrifuged; supernatants from both cycles were pooled. The combined supernatant was subjected to sequential centrifugation steps: first at 2,700 g for 10 min at 4°C, followed by re-suspension and re-centrifugation of the pellet under identical conditions. The pooled supernatants were further centrifuged at 37,000 g for 20 min. After discarding the supernatant and reddish layer on top of the pellet, the remaining pellet was gently re-suspended in a minimal volume of HB buffer (<5 mL) and maintained on ice as the light mitochondrial (LM) fraction.

OptiPrep density gradients (1.12, 1.15, 1.19, 1.22, and 1.26 g/mL) were prepared by diluting 60% OptiPrep stock solution (1.32 g/mL; Sigma-Aldrich) with GB buffer (5 mM MOPS, 1 mM EDTA, 2 mM PMSF, 1 mM DTT, pH 7.4). Using 13.2 mL ultracentrifuge tubes (Beckman Coulter Inc.), gradients were layered sequentially in decreasing density order (1.26–1.12 g/mL) with volumes of 1, 0.75, 1.5, 1.75, and 2.5 mL, respectively. Subsequently, 5 mL of the light mitochondrial fraction was layered on top of the gradient. Centrifugation was performed using an SW 41 Ti rotor (Beckman Coulter) at 33,000 *gmax* for 53 min. Following centrifugation, peroxisomes were predominantly localized in the lower three bands, which were carefully aspirated. The collected fractions were diluted 1:4 (v/v) with HB buffer and pelleted by centrifugation at 37,000 g for 15 min. The final pellet was re-suspended in a minimal volume (100–200 µL) of lysis buffer (20 mM Tris, 150 mM NaCl, pH 8.0) or HB buffer supplemented with 0.25% Triton X-100 (v/v) for single-particle analysis (SPA) sample preparation and biochemical assays.

Single-particle Cryo-EM sample preparation

For purified UOX protein samples without its substrate UA, the cryo-EM holey carbon grids (Quantifoil, R2/1, Au, 200 mesh) were glow-discharged before plunge freezing using an FEI Vitrobot IV with 100% humidity and 4°C. Around 4 µL aliquots of the

Langtaosha (LTS) Preprint doi: https://doi.org/10.65215/LTSpreprints.2026.04.18.000189. This version posted April 18, 2026. The copyright holder for this preprint (which was not certified by peer review) is the author/funder. Creative Commons license: CC Attribution-NonCommercial-NoDerivatives 4.0 https://creativecommons.org/licenses/by-nc-nd/4.0

prepared protein samples (~1 mg/mL) were applied to the grids, and blotted with a force of 0 and time of 3 s before plunge freezing in liquid ethane.

For purified UOX protein samples with its substrate UA, the cryo-EM holey carbon grids (Quantifoil, R1.2/1.3, Cu, 200 mesh) were glow-discharged before plunge freezing using an FEI Vitrobot IV with 100% humidity and 4°C. Protein samples were concentrated to approximately 1 mg/mL in lysis buffer (20 mM Tris, 150 mM NaCl, pH 8.0) saturated with UA. To ensure saturation was maintained, additional UA was supplemented prior to sample preparation. Around 4 μL aliquots were applied to the grids, and blotted with a force of 0 and time of 3 s before plunge freezing in liquid ethane.

For isolated peroxisomes from mouse livers, the cryo-EM holey carbon grids (Quantifoil, R2/1, Cu, 200 mesh) were glow-discharged before plunge freezing using an FEI Vitrobot IV with 50% humidity and 4°C. Around 4 μL aliquots of the peroxisome samples were applied to the grids, and blotted with a force of 0 and time of 5 s before plunge freezing in liquid ethane.

Single-particle Cryo-EM data acquisition

For purified UOX protein samples without its substrate UA, the cryo-EM data was acquired in the 300 kV Titan Krios G4 microscope equipped with a Selectris X energy filter using the EPU software (Thermo), with a nominal magnification of 165,000× (pixel size: 0.74 Å) and a defocus range of -1.0 to -1.4 μm. The images were recorded using a Thermo Falcon 4 camera with counted mode in EER format, with a dose rate of 15.41 $e^-/s/Å^2$, a total dose of 60 $e^-/Å^2$, a total exposure time of 3.90 s, and a total frame of 938.

For purified UOX protein samples with its substrate UA, the cryo-EM data was acquired in the 300 kV Titan Krios G4 microscope equipped with a Selectris X energy filter using the EPU software (Thermo), with a nominal magnification of 165,000×

Langtaosha (LTS) Preprint doi: https://doi.org/10.65215/LTSpreprints.2026.04.18.000189. This version posted April 18, 2026. The copyright holder for this preprint (which was not certified by peer review) is the author/funder. Creative Commons license: CC Attribution-NonCommercial-NoDerivatives 4.0 https://creativecommons.org/licenses/by-nc-nd/4.0

(pixel size: 0.74 Å) and a defocus range of -1.0 to -1.4 μm. The images were recorded using a Thermo Falcon 4 camera with counted mode in EER format, with a dose rate of 17.71 $e^-/s/Å^2$, a total dose of 60 $e^-/Å^2$, a total exposure time of 3.38 s, and a total frame of 812.

For isolated peroxisomes from mouse livers, the cryo-EM data was acquired in the 200 kV Glacios2 microscope equipped with a Selectris X energy filter using the EPU software (Thermo), with a nominal magnification of 130,000× (pixel size: 0.93 Å) and a defocus range of -1.0 to -2.0 μm. The images were recorded using a Thermo Falcon 4 camera with counted mode in EER format, with a dose rate of 11.09 $e^-/s/Å^2$, a total dose of 60 $e^-/Å^2$, a total exposure time of 5.41 s, and a total frame of 1302.

Single-particle Cryo-EM image processing

For purified UOX without UA, images were processed in RELION/4.0 [98]. A total of 19,264 dose-fractionated movies were motion-corrected using RELION's implementation of MotionCor2, followed by CTF estimation with CTFFIND4 [99]. After selection, 14,858 micrographs were retained for further processing. Particles were template-picked using a 3D reference (PDB: 4MB8) and curated via several rounds of 2D classification. Selected particles underwent 3D classification with D2 symmetry. The best class, containing 101,075 particles, was subjected to 3D auto-refinement, CTF refinement, and Bayesian polishing [100]. The final map reached a resolution of 2.79 Å based on the gold-standard FSC = 0.143 criterion [101]. Map quality was further improved using DeepEMhancer [102], and local resolution was estimated in RELION. Directional FSC and sphericity were calculated using 3DFSC [103].

For purified UOX with UA, images were processed in cryoSPARC version 4.6.0 [104]. A total of 22,739 movies were aligned via patch motion correction, and CTF parameters were estimated using patch CTF. Following curation, 13,402 micrographs were selected. Particles were picked using both template matching and Topaz [105], then cleaned via reference-free 2D classification. Selected particles underwent heterogeneous

Langtaosha (LTS) Preprint doi: https://doi.org/10.65215/LTSpreprints.2026.04.18.000189. This version posted April 18, 2026. The copyright holder for this preprint (which was not certified by peer review) is the author/funder. Creative Commons license: CC Attribution-NonCommercial-NoDerivatives 4.0 https://creativecommons.org/licenses/by-nc-nd/4.0

refinement using an ab initio reconstruction as the initial model. The best class was iteratively optimized through non-uniform refinement [106], orientation rebalancing and heterogeneous refinement. The final reconstruction, comprising 304,325 particles, reached a resolution of 2.42 Å (FSC = 0.143). The map was post-processed with DeepEMhancer. Local resolution and anisotropy were assessed using cryoSPARC and Orientation Diagnostics, respectively.

For isolated peroxisome samples, images were processed in cryoSPARC version 4.6.0 and RELION/5.0. A total of 3,929 movies were aligned via patch motion correction, and CTF parameters were estimated using patch CTF in cryoSPARC. A subset of 888 micrographs containing distinct UOX fibers was manually selected and imported into RELION 5.0. Fibers were manually picked by defining start-end coordinates and extracted with an inter-box distance of 70 Å and a box size of 428 Å. Following three rounds of 2D classification (binned by 2), a subset of particles was subjected to 3D auto-refinement to optimize helical parameters (twist = -144.095°, rise = 15.52 Å). Particles were then imported back into cryoSPARC and re-extracted without binning. Non-uniform refinement was performed using a subtomogram averaging map as the initial reference, followed by helical refinement. After CTF refinement and reference-based motion correction, helical refinement was applied with D1 symmetry, and duplicates were removed based on a minimum distance of 30 Å. Finally, symmetry expansion was performed using the final helical parameters (twist = -144.11°, rise = 15.52 Å), followed by local refinement masked to the central 40% of the fiber. This yielded a final map at 3.64 Å resolution comprising 219,322 particles. Map quality was improved using EMReady [107],and local resolution was estimated using in cryoSPARC.

Model building and refinement

Atomic models were initially generated using model-angelo [108] or cryoNet [109] based on maps post-processed using DeepEMhancer or EMReady. These models were manually adjusted with Coot [110]. The model of the UOX-UA complex was derived from the apo-UOX structure, while the UOX fiber model was built upon the UA-complexed UOX

Langtaosha (LTS) Preprint doi: https://doi.org/10.65215/LTSpreprints.2026.04.18.000189. This version posted April 18, 2026. The copyright holder for this preprint (which was not certified by peer review) is the author/funder. Creative Commons license: CC Attribution-NonCommercial-NoDerivatives 4.0 https://creativecommons.org/licenses/by-nc-nd/4.0

structure. All final models were refined using phenix.real_space_refine[111,112] with geometric constraints and validated using MolProbity[113]. Figures of cryo-EM density maps and analyses of molecular interactions were prepared using ChimeraX, Chimera [114] and PyMOL [115].

Western blotting

For detection of UOX during peroxisome isolation, 10 μL of aliquots from each centrifugation stage and Optiprep gradient fraction were loaded for SDS-PAGE (10% w/v) analysis and transferred to PVDF membranes. Membranes were blocked and incubated with primary antibodies (uricase 1:500; sc-166214, Santa Cruz Biotechnology) followed by incubation with an HRP-conjugated goat anti-mouse IgG secondary antibody (1:25,000, HA1006, HUABIO). Chemiluminescent signals were captured using a Tanon-5200 Imaging System.

For determination of UOX abundance in activity assays, total protein concentrations of purified UOX and lysed peroxisomes were determined using BCA protein assay kit (Thermo Fisher Scientific). For each sample, approximately 0.5 μg of total protein was loaded in triplicate onto SDS-PAGE gels for immunoblotting, as described above. Band intensities were quantified via integrated density analysis using ImageJ (NIH). These values were subsequently used to normalize the specific activity of UOX across samples. Data analysis and visualization were performed using GraphPad Prism (v9.0), with results expressed as mean ± SD from three technical replicates. All experiments were independently repeated three times to ensure biological reproducibility.

For pelleting assay of UOX in peroxisomes, lysed peroxisomes were centrifuged at 25,000×g for 15 min at 4°C. The resulting supernatant and pellet fractions were separated, with the pellet resuspended in a volume of HB buffer equivalent to the supernatant. Equal volumes of the total peroxisome lysate, supernatant, and pellet fractions were analyzed by western blotting under identical conditions. Band intensities were quantified via integrated density analysis using ImageJ (NIH), and data were

Langtaosha (LTS) Preprint doi: https://doi.org/10.65215/LTSpreprints.2026.04.18.000189. This version posted April 18, 2026. The copyright holder for this preprint (which was not certified by peer review) is the author/funder. Creative Commons license: CC Attribution-NonCommercial-NoDerivatives 4.0 https://creativecommons.org/licenses/by-nc-nd/4.0

907 normalized to the mean density of peroxisome samples. Graphs were generated in
908 GraphPad Prism (v9.0). Means and error bars represent the average and standard
909 deviation (SD) of triplicate lane measurements, respectively. Ratios of normalized
910 values were calculated using error propagation formulas to determine mean and SD.
911 All experiments were independently repeated three times to ensure biological
912 reproducibility.
913
914 **UOX activity assay**
915 The UOX enzymatic activity was determined spectrophotometrically by monitoring the
916 decrease of uric acid by following the absorbance at 293 nm (A293). A freshly prepared
917 1 mM uric acid stock in lysis buffer (20 mM Tris, 150 mM NaCl, pH 8.0), was diluted
918 with lysis buffer to prepare a uric acid concentration of 300 μM. The concentration of
919 all UOX samples was determined by the BCA protein assay kit (Thermo Fisher
920 Scientific). For each assay, 200 μL of uric acid solution was dispensed into individual
921 wells of a 96-well plate and pre-incubated at 37°C. Prior to initiating the reaction, 10
922 μL of enzyme solution (total protein concentration: 0.1 mg/mL) or buffer alone was
923 added to each well. Absorbance changes at 293 nm were recorded every minute for 20
924 min at 37°C using a microplate reader. The specific activity for all UOX samples was
925 defined as the amount of uric acid substrate (in μM) oxidized per minute per milligram
926 of total protein.
927
928 **Determination of kinetic parameters**
929 A freshly prepared 1 mM uric acid stock in lysis buffer (20 mM Tris, 150 mM NaCl,
930 pH 8.0), was diluted with lysis buffer to prepare a range of uric acid concentrations.
931 Specifically, the assays were performed at the following uric acid concentrations: 10
932 μM, 20 μM, 30 μM, 50 μM, 75 μM, 100 μM, 150 μM, and 200 μM. Each experiment
933 included triplicate technical replicates, and three independent biological replicates were
934 performed. The average initial reaction rates from triplicate samples were used to fit
935 the Michaelis-Menten equation and calculate V_{max} and K_m values in GraphPad Prism
936 v9.0. The concentration of all UOX samples was determined by the BCA protein assay

Langtaosha (LTS) Preprint doi: https://doi.org/10.65215/LTSpreprints.2026.04.18.000189. This version posted April 18, 2026. The copyright holder for this preprint (which was not certified by peer review) is the author/funder. Creative Commons license: CC Attribution-NonCommercial-NoDerivatives 4.0 https://creativecommons.org/licenses/by-nc-nd/4.0

kit (Thermo Fisher Scientific). Catalytic efficiency (k_{cat}) was derived by dividing V_{max} by the total enzyme concentration. The data are presented as the mean ± standard deviation (SD) of at least three independent experiments.

Thermostability analysis

The purified UOX and isolated, lysed peroxisomes were quantified using the BCA protein assay kit (Thermo Fisher Scientific) to get a concentration of 0.1 mg/mL before incubating for 3 min at various temperatures (40,45,50,55,60,65,70,80,90℃). Then they were transferred on ice for at least 10 min before the residual enzymatic activity was assayed using the method described above. The activity was measured in triplicate technical replicates for each sample and was normalized to the untreated control (0℃ heat treatment) to account for baseline variations. The decline in enzymatic activity as a function of temperature was fitted using nonlinear regression with a sigmoidal dose-response model in GraphPad Prism v9.0. The melting temperature (Tm) for each sample was defined as the temperature at which 50% of enzymatic activity was lost relative to the untreated control.

Proteinase K resistance assay

Proteinase K resistance assay was performed with the following reaction system: 90 μL sample (purified protein or isolated peroxisomes) was incubated with 9 μL Proteinase K solution (containing 9 μg sample proteins and 2.25 μg Proteinase K) at 37°C with shaking at 200 rpm. Reactions were terminated at time points of 0.5, 1, 1.5, and 2 h by adding phenylmethylsulfonyl fluoride (PMSF) to a final concentration of 1 mM. Untreated samples supplemented with 9 μL lysis buffer (20 mM Tris, 150 mM NaCl, pH 8.0) served as controls. Residual enzymatic activity was measured for all samples under identical parameters as described for the UOX activity assay, with at least three technical replicates per time point.

UOX mutant structure prediction

The UOX mutant used in this paper was created by replacing the loop corresponding to

Langtaosha (LTS) Preprint doi: https://doi.org/10.65215/LTSpreprints.2026.04.18.000189. This version posted April 18, 2026. The copyright holder for this preprint (which was not certified by peer review) is the author/funder. Creative Commons license: CC Attribution-NonCommercial-NoDerivatives 4.0 https://creativecommons.org/licenses/by-nc-nd/4.0

amino acids 200-206 with the one from *Aspergillus flavus* homolog. The full-length sequence of mutant UOX was used to predict its structure using AlphaFold3 [116].

Quantification and statistical analysis

The activity curves were generated by averaging triplicate measurements, with error bars representing ± standard deviation (SD). All fitting parameters, including kinetic parameters and Tm values, were derived from at least three independent biological replicates to ensure reproducibility. Statistical comparisons between purified UOX tetramers and UOX assembly from peroxisome samples were performed using Welch's unpaired *t*-tests obtained from technical triplicates across biological replicates.

Animals

All animal housing and use procedures were approved by the Institutional Animal Care and Use Committees of Peking University, an AAALAC accredited laboratory animal facility. All mice used in the experiments were provided by Peking University and bred on the C57BL/6J background. All rats used in the experiments were Wistar IGS background purchased from Vital River Laboratory Animal Technology Co., Ltd. *Uox* liver knockout (KO) mice were obtained by intravenous injecting spCas9 mice with AAV 2/8 carring TBG-Cre and *Uox* targeting sgRNA. Cre-dependent spCas9 knockin (KI) mice were purchased from the Jackson Lab (RRID: IMSR_JAX: 026556). Mice were housed under standardized conditions, including a temperature of approximately 22˚C, a 12 h light/dark cycle, and humidity of 40%-60%. Mice had free access to food and water unless otherwise stated. Mice aged 6 weeks were used in all experiments. Mice were randomly assigned to different experimental groups.

DNA vector construction

For CRISPR/Cas9-mediated acute knockout of UOX in mouse liver, pX602-AAV-Cre-sgRNA plasmid was edited from pX602 (Addgene, 61593) vector according to previously reported procedures[117]. In brief, sequence of Cre recombinase was inserted after the TBG promoter region, with the sequence of human U6 promoter and spCas9

Langtaosha (LTS) Preprint doi: https://doi.org/10.65215/LTSpreprints.2026.04.18.000189. This version posted April 18, 2026. The copyright holder for this preprint (which was not certified by peer review) is the author/funder. Creative Commons license: CC Attribution-NonCommercial-NoDerivatives 4.0 https://creativecommons.org/licenses/by-nc-nd/4.0

997 sgRNA-scaffold cloned into the same vector. The sgRNA sequence was designed by
998 the Benchling website. sgRNA 5'-tgtcggaattatcaccgtgt-3' was used for *Uox* gene
999 knockout in mouse liver. For UOX (WT/mutant) rescue in mouse liver, the cDNA
1000 sequence of FLAG-UOX (WT/mutant) were inserted into AAV-TBG-cDNA vector
1001 which was generated from AAV-TBG-GFP (Addgene, 105535). To avoid sgRNA-
1002 guided editing in UOX expression plasmids, the PAM region of sgRNA was mutated in
1003 an amino acid synonymous mutation form.
1004
1005 **Adeno-Associated Virus (AAV) production and delivery**
1006 HEK293T cells were used for AAV packaging. In brief, Rep/Cap (2/8) plasmids, delta-
1007 F6 plasmids and AAV shuttle vector plasmids were transfected into 293T cells by using
1008 PEI according to the manufacturer's instructions. Cells were scraped from culture
1009 dishes at 48 h after transfection. Viruses were purified by using Optiprep density
1010 gradient ultracentrifugation and quantified by qPCR of virus genome as previous
1011 reported[117]. For AAV delivery, tail vein injection was used into 6-week-old C57BL/6J
1012 mice. 4E11 viral genome copies of pX602-AAV-Cre-sgRNA were used for UOX
1013 knockout. For rescue experiments, 1E11 viral genome copies of AAV-TBG-FLAG-
1014 UOX (WT/mutant) were used together with 4E11 sgRNA virus.
1015
1016 **Serum uric acid detection**
1017 Blood samples were collected from wild-type mice, UOX liver-specific knockout (LKO)
1018 mice, and UOX (WT / mutant) rescue mice under ad libitum feeding conditions. Plasma
1019 was obtained by centrifuging the blood at 6,000 rpm for 5 min at 4°C, and the resulting
1020 supernatant (serum) was separated. Serum uric acid levels were measured using Uric
1021 Acid (UA) Colorimetric Assay Kit (E-BC-K016-M).
1022
1023 **Primary hepatocyte isolation**
1024 Primary hepatocytes were isolated from FLAG-UOX (WT / mutant) expressed UOX
1025 KO mice at 4 weeks post AAV injection. In brief, mice were anesthetized by 1% Pell-
1026 tobarbitalum Natricum (AMRESCO, USA), and then its liver was perfused with Krebs

Langtaosha (LTS) Preprint doi: https://doi.org/10.65215/LTSpreprints.2026.04.18.000189. This version posted April 18, 2026. The copyright holder for this preprint (which was not certified by peer review) is the author/funder. Creative Commons license: CC Attribution-NonCommercial-NoDerivatives 4.0 https://creativecommons.org/licenses/by-nc-nd/4.0

Ringer with Glucose (KRG) buffer to remove blood, followed by type IV collagenase (C5138, Sigma) containing KRG buffer to digest collagens. Then mouse liver was harvested and cut into pieces, and filtered through a 70 μm cell strainer (352350, Falcon) to remove tissue debris. The hepatocytes were separated by 3 times 50 g centrifugation for 4 min. The cell pellet was resuspended in DMEM containing 10% FBS and 1% P/S, and cultured at 37℃, 5% CO_2.

UOX purification from mouse primary hepatocytes

FLAG-UOX (WT/mutant) expressed primary hepatocytes were treated with DMSO/10 mM 3-AT (A601149-0025, BBI) containing DMEM for 12 h. Cells were washed with PBS twice and then scraped from dishes in buffer C (50 mM Tris pH=7.5, 150 mM NaCl, 1% TritonX-100, 1 mM EDTA-NaOH pH=8.0, 10% glycerol with protease inhibitors). The lysate was centrifuged at 12000 rpm for 10 min at 4℃, and the supernatants were used for FLAG IP. 50 μL FLAG agarose beads were incubated with the lysate for 2 h at 4℃ to enrich FLAG-UOX. Then, the FLAG beads were washed with the buffer C for 6 times and 150 μL 0.5 mg/mL FLAG peptide dissolved in buffer C were used to elute FLAG-UOX from beads. The eluate was further diluted with 5 mL TBS buffer (20 mM Tris, 150 mM NaCl, pH 7.5) and concentrated by using Amicon 5 mL concentrators (10 kDa cutoffs). The final product was quantified by BCA protein assay kit.

IAA-alkyne labeling of free cystines in UOX

10 μL 1 mg/mL FLAG-UOX were mixed with 10 μL 0.8% SDS dissolved in PBS at room temperature for 10 min to denature UOX and fully expose cystines. IAA-alkyne was used to label free cystines[118]. DMSO dissolved IAA-alkyne was added to protein solution at 5 mM final concentration and the mixture was incubated at room temperature for 30 min. 100 μL methanol-chloroform solution were added to reaction mixture and vortex 10 s to precipitate proteins from the mixture. Proteins were separated by 12000 rpm centrifugation at 4℃ for 10 min. The protein precipitates were washed by ice-cold methanol and then resuspended in 20 μL 0.4% SDS in PBS with

Langtaosha (LTS) Preprint doi: https://doi.org/10.65215/LTSpreprints.2026.04.18.000189. This version posted April 18, 2026. The copyright holder for this preprint (which was not certified by peer review) is the author/funder. Creative Commons license: CC Attribution-NonCommercial-NoDerivatives 4.0 https://creativecommons.org/licenses/by-nc-nd/4.0

sonication. IAA-alkyne labeled proteins were clicked with 200 μM Cy5-azide (777323, Sigma) or biotin-azide (T41046, TargetMol) at 29℃ for 30 min. The reaction solutions were mixed with 4× loading and subjected to SDS-PAGE followed by fluorescence imaging and immunoblot.

EM samples preparation and imaging

Animal samples were fixed at room temperature for 2 hours using 2.5% glutaraldehyde (#G5882, Sigma-Aldrich) in 0.1 M PB buffer (pH 7.4). Following four 10-minute washes with 0.1 M PB, samples were post-fixed with 1% OsO_4 in 0.1 M PB containing 0.8% $K_4Fe(CN)_6$ for one hour in the dark. They were then rinsed again extensively with ultrapure water. Dehydration was carried out through a graded ethanol series (30%, 50%, 70%, 85%, 95%, and 100%; 6 minutes per step) and two changes of acetone (100%, 8 minutes each). The tissue blocks were then infiltrated gradually with EMbed 812 resin (#14120, Electron Microscopy Sciences). Polymerization of the resin was performed at 65 °C for 24 hours. The resin blocks were trimmed and sectioned with an ultramicrotome (UC7, Leica Microsystems) using a diamond knife (Ultra 35°, Diatome, Switzerland). Ultrathin sections (75 nm) were collected on formvar-film-coated single-slot grids, stained with uranyl acetate and lead citrate, and examined under a transmission electron microscope (Tecnai G2 Spirit BioTWIN, FEI) operating at 120 kV. Digital images were acquired with a Gatan 832 CCD camera (Gatan, Pleasanton, CA).

Quantum mechanics/Molecular mechanics simulation

The initial conformation for the MD simulations was taken from the cryo-EM–resolved tetrameric structure of UOX. Protons are added to the structure with PDBFixer toolkit[119] and Open Babel [120]. The periodic water box and neutralizing ions were constructed using the tleap module. The ff14SB force field [121] was applied to the protein, while the TIP3P[122] model was used for water molecules and ions. All molecular dynamics simulations were performed with the Amber20 [123] software package.

Langtaosha (LTS) Preprint doi: https://doi.org/10.65215/LTSpreprints.2026.04.18.000189. This version posted April 18, 2026. The copyright holder for this preprint (which was not certified by peer review) is the author/funder. Creative Commons license: CC Attribution-NonCommercial-NoDerivatives 4.0 https://creativecommons.org/licenses/by-nc-nd/4.0

A positional restraint with a force constant of 5.0 kcal/mol was first applied to the protein and reactant molecules during 5000 steps of energy minimization, followed by another minimization of 1000 steps with a reduced force constant of 2.0 kcal/mol. Simulations were carried out at a temperature of 300 K and a pressure of 1 bar. To prevent the small molecules from diffusing out of the binding pocket, an additional positional restraint with a force constant of 2.0 kcal/mol was applied. The system then underwent a 100 ps heating phase, a 100 ps pressure equilibration, and a 2 ns equilibration run, resulting in the MD-equilibrated structure of UOX in complex with its substrate. The RMSD calculations in this section were performed with reference to the initial structure of UOX in complex with the reactant substrate. The interface residues used for RMSD calculations were defined as the heavy atoms of residues numbered 68–105, 119–131, 146–151, 199–206, and 267–281 in each monomer of the initial structure PDB file.

Subsequently, key intermediate and transition state structures reported in the reference[124] were aligned to the corresponding atoms of the system. The atomic coordinates of the intermediates, as reported in the literature, were fixed, and the resulting structures were subjected to the same 6000-step minimization protocol described above. Following minimization, a 100 ps equilibration simulation was performed using the QM/MM interface between sander in AmberTools [123] and ORCA[125,126], externally coupled with the xTB software package [127] employing the GFN2-xTB[128] semiempirical method for the QM region. In this section, RMSD calculations were carried out using the MD-equilibrated structure of UOX in complex with the reactant substrate as the reference, with interface residues defined in the same manner.

Sequence alignment and phylogenetic tree

For the sequence alignment of UOX among mammals that has been reported the presence of putative UOX-derived crystalloid inclusions, their amino acid sequences were downloaded from Uniprot before being aligned in CLUSTALW [129]

Langtaosha (LTS) Preprint doi: https://doi.org/10.65215/LTSpreprints.2026.04.18.000189. This version posted April 18, 2026. The copyright holder for this preprint (which was not certified by peer review) is the author/funder. Creative Commons license: CC Attribution-NonCommercial-NoDerivatives 4.0 https://creativecommons.org/licenses/by-nc-nd/4.0

(https://www.genome.jp/tools-bin/clustalw). The result was visualized in ESPript 3.0 [130].

For the sequence alignment of UOX in Chordata, the BLASTP search against UOX from the phylum Chordata was performed using the NCBI BLASTP model [131]. The RefSeq protein database [132] (refseq_protein) was selected as the reference, with an E-value threshold of < 1e−5. Hits with a query coverage below 70% were excluded. All retrieved sequences, along with the target UOX sequence, were aligned using MUSCLE (v3.8.31) [133] for multiple sequence alignment. Sequence logos were generated using WebLogo 3 [70].

Based on the alignment, the residue variations at 11 positions (100, 101, 123, 147, 148, 202, 203, 274, 275, 81, and 82) that may be involved in UOX assembly formation were analyzed. Phylogenetic relationships among the chordate species present in the RefSeq protein dataset were extracted from the Open Tree of Life [134] using the R package rotl (v3.1.0) [135]. Mutations known and inferred not to affect assembly formation (L81F, R82K, N148S, R202Q) were excluded from further analysis. The resulting phylogenetic tree was visualized and annotated with mutation profiles using the R package ggtree (v3.16.0) [136].

LC-MS/MS analysis of UOX oxidation

The protein samples were separated using SDS-PAGE (3-5 μg/lane). The gel slices were incubated with dithiothreitol (10 mM) at 37℃ for 1 h, then subsequently alkylated with iodoacetamide (20 mM) at 37℃ for 30 min in the dark. In-gel digestion was performed using trypsin, Glu-C and chymotrypsin (w:w = 1:40) at 37℃ for 16 h, respectively. After digestion, the resulting peptides were extracted from the gel using acetonitrile and subsequently lyophilized. The peptides were desalted using C18 columns (ThermoFisher, SOLAμ), eluted with acetonitrile (80% v/v) containing formic acid (0.1% v/v) and subsequently lyophilized.

The lyophilized tryptic peptides were reconstituted with formic acid (0.1% v/v) and

Langtaosha (LTS) Preprint doi: https://doi.org/10.65215/LTSpreprints.2026.04.18.000189. This version posted April 18, 2026. The copyright holder for this preprint (which was not certified by peer review) is the author/funder. Creative Commons license: CC Attribution-NonCommercial-NoDerivatives 4.0 https://creativecommons.org/licenses/by-nc-nd/4.0

injected into an LC-MS/MS system. This system consisted of an TimsTOF Pro mass spectrometer (Bruker) coupled to a NanoElute nano-LC system. The mobile phase was composed of water with formic acid (0.1% v/v) as solvent A and acetonitrile with formic acid (0.1% v/v) as solvent B. All samples were then separated on a 15 cm C18 analytical column (EVOSEP, EV-1106) at a passive split flow of 500 nL/min for 75 min. The separation using NanoElute nano-LC involved a linear gradient of 2-12% solvent B over 10 min, followed by 12-35% solvent B over 45 min, 35-45% solvent B over 10 min, 45-95% solvent B for 1 min and 95% solvent B for 9 min.

The raw LC-MS/MS data were processed with PEAKS Online (Bioinformatics Solutions). The data searched against a database containing target sequences. The search using PEAKS Online followed the standard sequence database search workflow. The precursor mass tolerance was set to 20 ppm and the fragment mass tolerance was set to 0.05 Da. The maximum number of missed cleavages was set to 1. The maximum number of modifications was set to 5. Carbamidomethylation of cysteine was defined as fixed modification. The variable modifications included:

1) oxidation of any residues (MW +15.99 Da)
2) oxidation of cysteine (MW +47.98 Da, -15.99 Da, +31.98 Da)
3) oxidation of tryptophan, tyrosine and phenylalanine (MW +31.98 Da)
4) oxidation of methionine (MW +31.98 Da, -31.98 Da)
5) oxidation of histidine (MW -21.99 Da)
6) oxidation of arginine (MW -42.99 Da, +13.99 Da)
7) oxidation of isoleucine, leucine, valine, proline glutamine and glycine (MW +13.99 Da)
8) oxidation of glutamic acid (MW -29.99 Da, +13.99 Da)
9) oxidation of aspartic acid (MW +29.99 Da)

Langtaosha (LTS) Preprint doi: https://doi.org/10.65215/LTSpreprints.2026.04.18.000189. This version posted April 18, 2026. The copyright holder for this preprint (which was not certified by peer review) is the author/funder. Creative Commons license: CC Attribution-NonCommercial-NoDerivatives 4.0 https://creativecommons.org/licenses/by-nc-nd/4.0

Figure Legends of Extended Data Figures and Tables

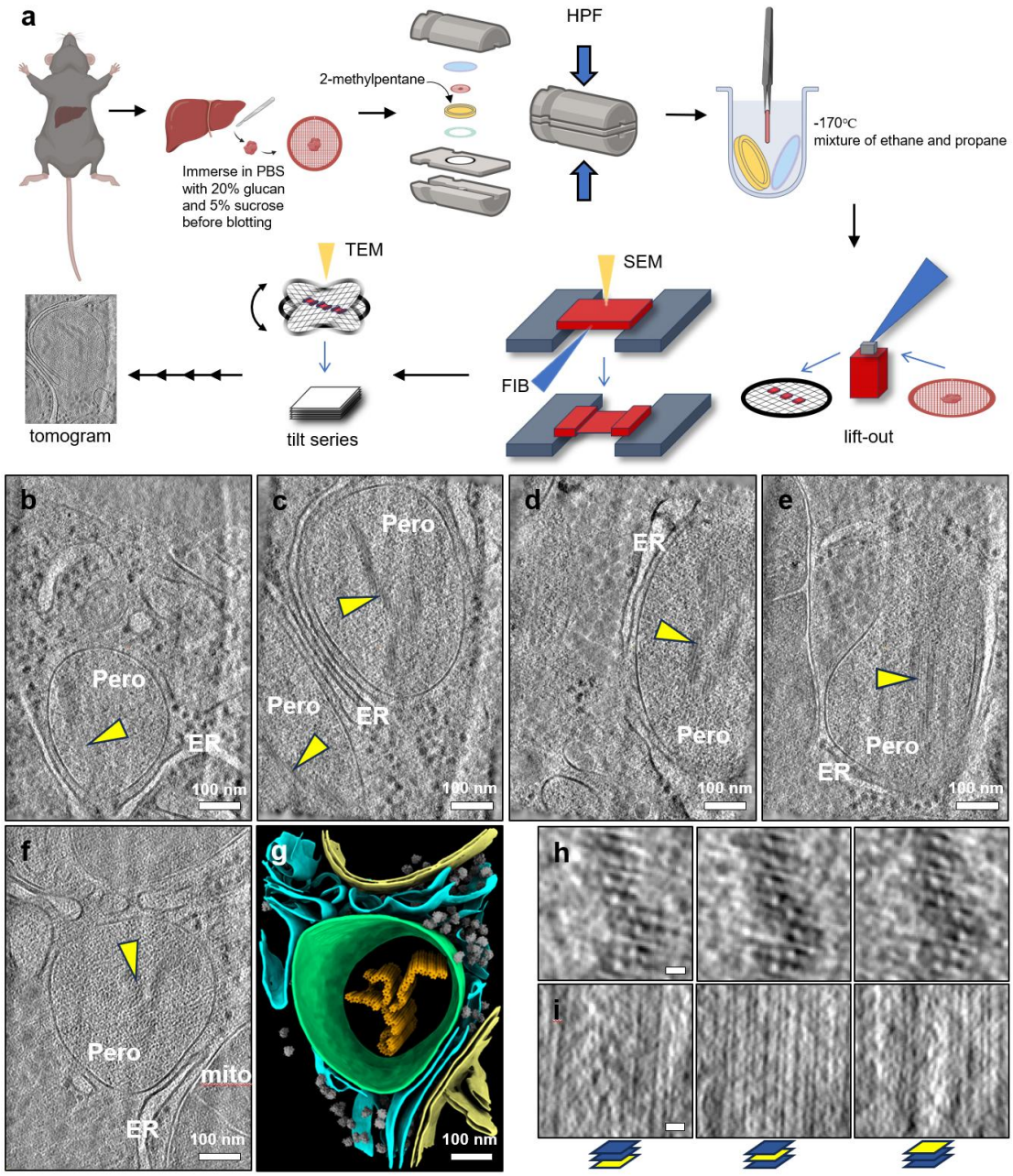

Supplementary Figure 1: Cryo-electron tomography of mouse liver tissue.

a, Workflow for cryo-electron tomography sample preparation for tissues and data acquisition from mouse liver tissues.

b-f, Representative tomograms acquired from mouse livers prepared from the workflow in (**a**). Yellow arrowheads indicate the supramolecular UOX assembly. Pero, peroxisome. Scale bars, 100 nm.

Langtaosha (LTS) Preprint doi: https://doi.org/10.65215/LTSpreprints.2026.04.18.000189. This version posted April 18, 2026. The copyright holder for this preprint (which was not certified by peer review) is the author/funder. Creative Commons license: CC Attribution-NonCommercial-NoDerivatives 4.0 https://creativecommons.org/licenses/by-nc-nd/4.0

g, 3D rendering of the segmentation from the tomogram shown in (**f**). Yellow, mitochondrion. Magenta, ER membrane. Grey, ribosome. Green, peroxisome. Orange, the UOX assembly. Scale bars, 100 nm.

h-i, Different Z-axis slices of the UOX assembly at the top (**h**) and side (**i**) views from tomograms. Scale bars, 10 nm.

Langtaosha (LTS) Preprint doi: https://doi.org/10.65215/LTSpreprints.2026.04.18.000189. This version posted April 18, 2026. The copyright holder for this preprint (which was not certified by peer review) is the author/funder. Creative Commons license: CC Attribution-NonCommercial-NoDerivatives 4.0 https://creativecommons.org/licenses/by-nc-nd/4.0

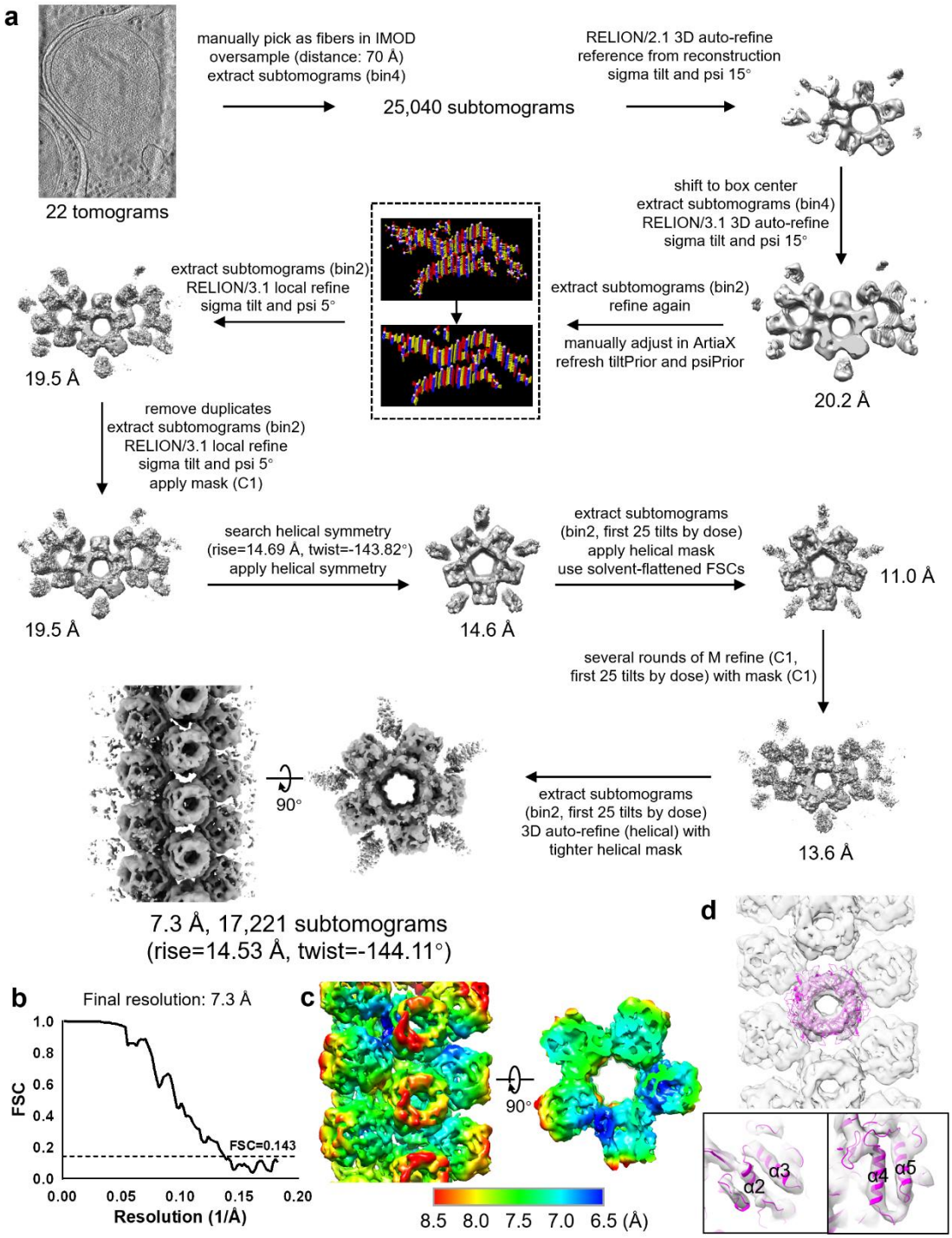

Supplementary Figure 2: The subtomogram averaging of mouse UOX assembly

a, Workflow of subtomogram averaging of mouse UOX assembly.

b, Fourier shell correlation (FSC) curve of final map where FSC = 0.143 is used as a cutoff to estimate resolution.

c, Final density map colored according to local resolution (Å) as indicated by the color bar. Left, side view. Right, top view.

Langtaosha (LTS) Preprint doi: https://doi.org/10.65215/LTSpreprints.2026.04.18.000189. This version posted April 18, 2026. The copyright holder for this preprint (which was not certified by peer review) is the author/funder. Creative Commons license: CC Attribution-NonCommercial-NoDerivatives 4.0 https://creativecommons.org/licenses/by-nc-nd/4.0

d, (Top) Atomic model of mouse UOX predicted by AlphaFold2 fitted into the final density map. (Bottom) Representative fit of four α-helices highlighting agreement between model and density.

Langtaosha (LTS) Preprint doi: https://doi.org/10.65215/LTSpreprints.2026.04.18.000189. This version posted April 18, 2026. The copyright holder for this preprint (which was not certified by peer review) is the author/funder. Creative Commons license: CC Attribution-NonCommercial-NoDerivatives 4.0 https://creativecommons.org/licenses/by-nc-nd/4.0

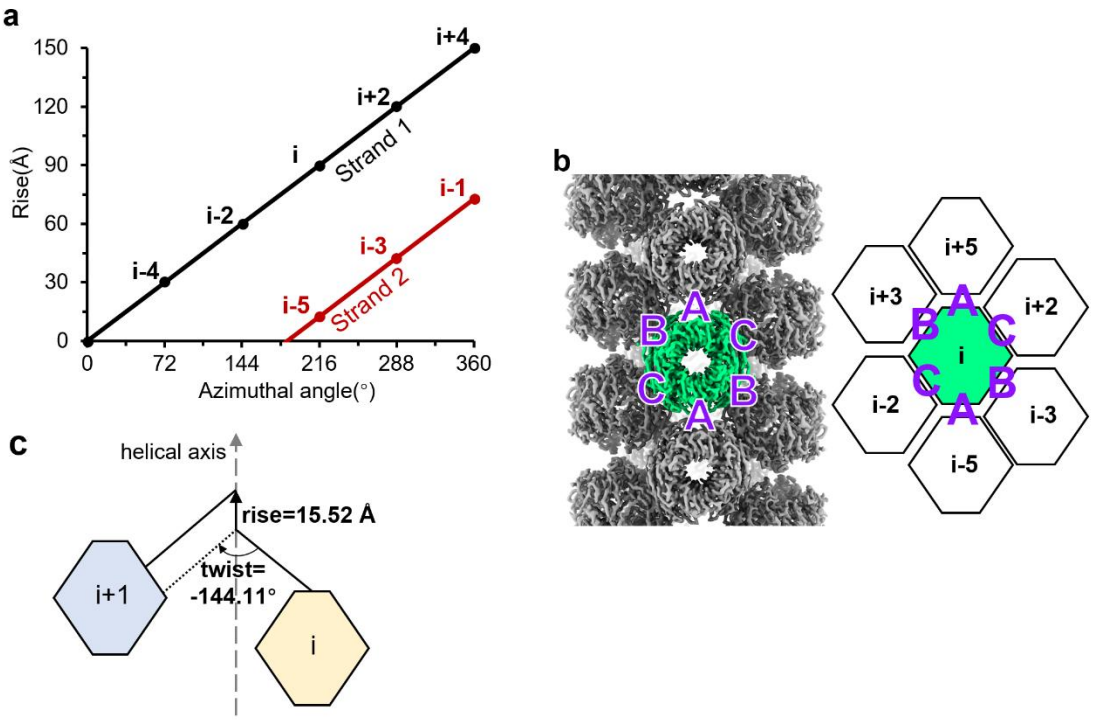

Supplementary Figure 3: Structural organization of the mouse UOX helical fiber.

a, 2D surface lattice plot of the UOX fiber, with z-height plotted against the azimuthal angle. The centers of individual subunits are represented as dots, with the two strands colored black and red. Subunit indices are annotated.

b, Left, high-resolution density map of UOX fibers with the subunit i colored green. Right, schematic of subunit i and its directly interacting neighbors. Three interfaces are labeled in blue as A, B, and C.

c, Relative orientation of subunit i and i+1, illustrating the helical twist and rise applied.

Langtaosha (LTS) Preprint doi: https://doi.org/10.65215/LTSpreprints.2026.04.18.000189. This version posted April 18, 2026. The copyright holder for this preprint (which was not certified by peer review) is the author/funder. Creative Commons license: CC Attribution-NonCommercial-NoDerivatives 4.0 https://creativecommons.org/licenses/by-nc-nd/4.0

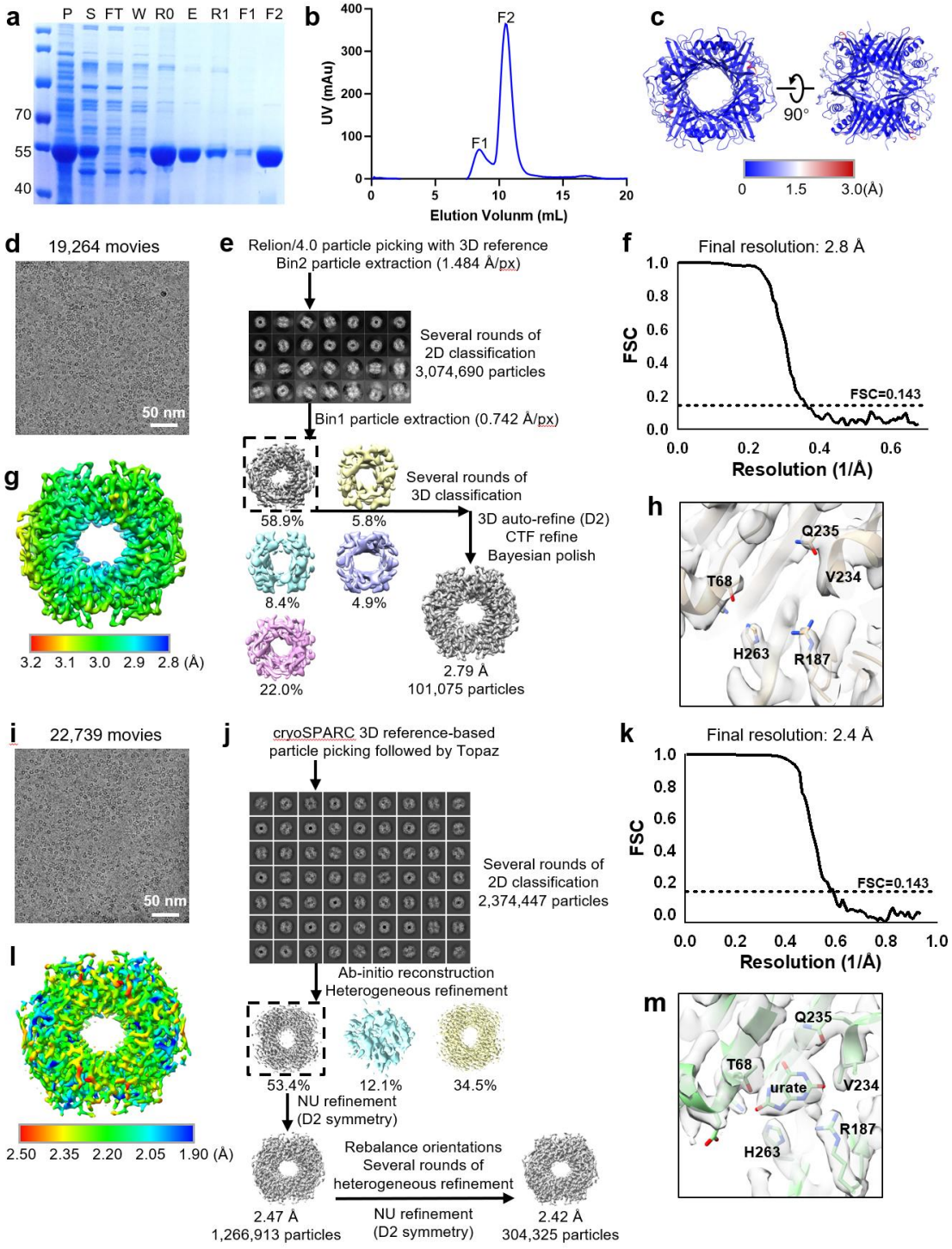

Supplementary Figure 4: Structure determination of mouse UOX tetramer in apo state and substrate-bound state.

a, SDS-PAGE with Coomassie Blue staining. Fraction 1 (F1) and fraction 2 (F2) are from size exclusion chromatography shown in (**b**). P, precipitation. S, supernatant. FT, flowthrough. W, wash. R0, resin before elution. E, eluate. R1, resin after elution.

b, Size exclusion chromatogram profile (Superdex 200 Increase 10/300 GL) of mouse

Langtaosha (LTS) Preprint doi: https://doi.org/10.65215/LTSpreprints.2026.04.18.000189. This version posted April 18, 2026. The copyright holder for this preprint (which was not certified by peer review) is the author/funder. Creative Commons license: CC Attribution-NonCommercial-NoDerivatives 4.0 https://creativecommons.org/licenses/by-nc-nd/4.0

UOX in the apo state.

c, Atomic model of the UOX tetramer colored by RMSD between the apo state and substrate-bound state.

(**d–h**) Refers to the cryo-EM processing of UOX in the apo state, and (**i–m**) in the substrate-bound state.

d, i, Representative micrographs.

e, j, Data processing workflow, including representative 2D class averages, 3D classification steps and final reconstructed map.

f, k, Fourier shell correlation (FSC) curves of final map where FSC = 0.143 (black line) is used as a cutoff to estimate resolution.

g, l, Final density map colored according to local resolution (Å) as indicated by the color bar.

h, m, Density of substrate-binding pocket and its neighboring residues, shown with the fitted atomic model.

Langtaosha (LTS) Preprint doi: https://doi.org/10.65215/LTSpreprints.2026.04.18.000189. This version posted April 18, 2026. The copyright holder for this preprint (which was not certified by peer review) is the author/funder. Creative Commons license: CC Attribution-NonCommercial-NoDerivatives 4.0 https://creativecommons.org/licenses/by-nc-nd/4.0

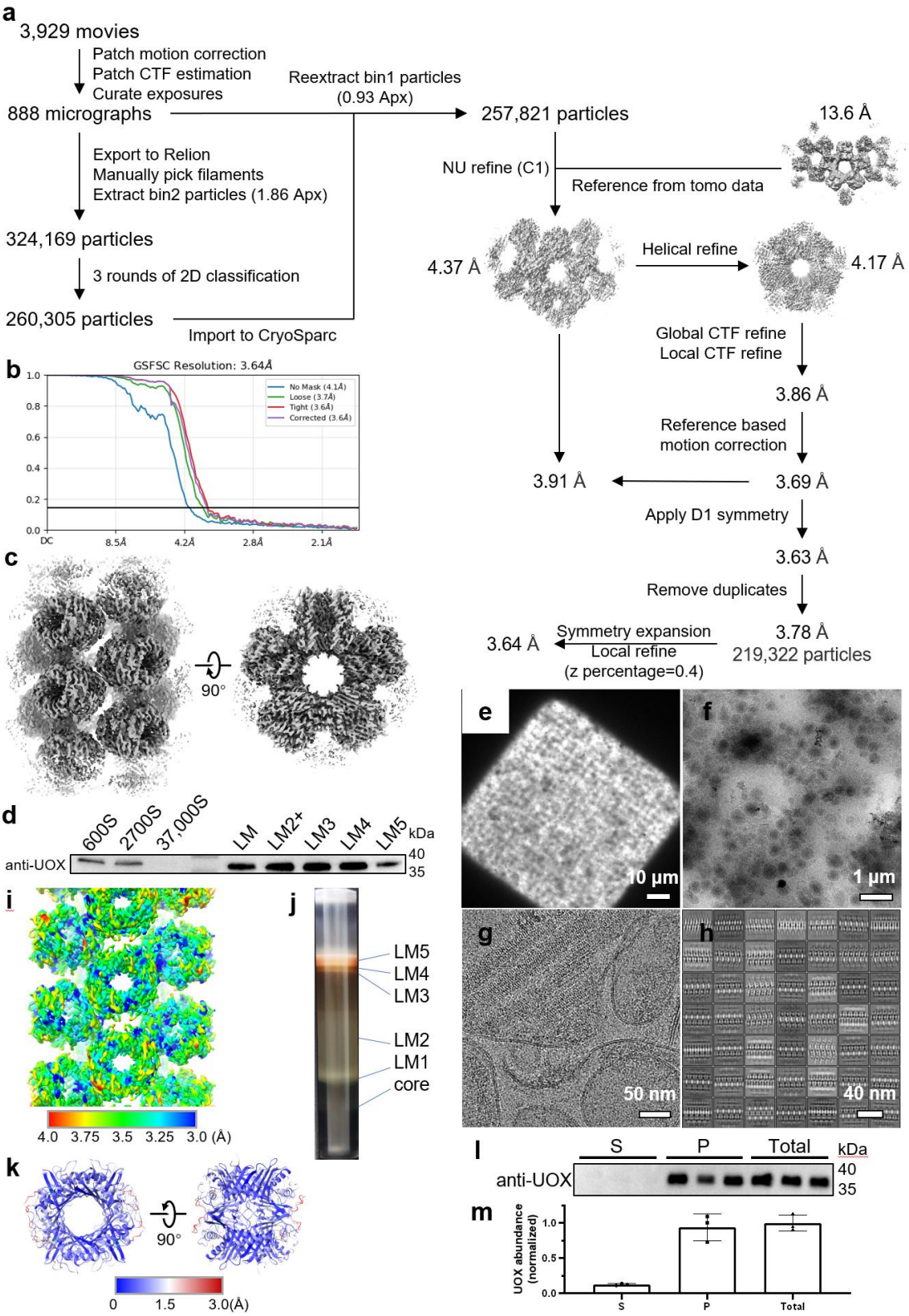

Supplementary Figure 5: Isolation of mouse peroxisomes and single-particle cryo-EM structure determination of UOX assembly.

a, Data processing workflow for the mouse UOX assembly, including 2D class averages and 3D refinement steps.

Langtaosha (LTS) Preprint doi: https://doi.org/10.65215/LTSpreprints.2026.04.18.000189. This version posted April 18, 2026. The copyright holder for this preprint (which was not certified by peer review) is the author/funder. Creative Commons license: CC Attribution-NonCommercial-NoDerivatives 4.0 https://creativecommons.org/licenses/by-nc-nd/4.0

b, Fourier shell correlation (FSC) curves of final map where FSC = 0.143 (black line) is used as a cutoff to estimate resolution.

c, Final density map of a single UOX fiber within the assembly, shown in side (left) and top (right) views.

d, Western blot analysis of UOX from fractions collected after Optiprep density gradient centrifugation. 600S, 2700S, and 37000S denote supernatants from sequential centrifugations of mouse liver homogenate at 600 g, 2,700 g, and 37,000 g, respectively. LM, sample loaded onto the gradient; LM2+, combined LM1-LM2 and core fractions.

e, Low-magnification view of a grid square with isolated peroxisomes. Scale bars, 10 μm.

f, Representative image of grid holes containing isolated peroxisomes. Scale bars, 1 μm.

g, Representative cryo-EM micrograph of isolated peroxisomes. Scale bars, 50 nm.

h, Representative 2D classification results of the UOX assembly. Scale bars, 40 nm.

i, Final density map colored according to local resolution (Å) as indicated by the color bar.

j, Visual representation of layers (core, LM1-LM5) after Optiprep density gradient centrifugation.

k, Atomic model of the UOX tetramer colored by RMSD between free tetramers and assembly-incorporated tetramers.

l, Western blot of UOX in different fractions of isolated peroxisomes after pelleting. S, supernatant. P, precipitation. Total, samples before centrifugation.

m, Quantification of band intensities from (**l**). Data are presented as mean ± SD; individual points represent technical replicates.

Langtaosha (LTS) Preprint doi: https://doi.org/10.65215/LTSpreprints.2026.04.18.000189. This version posted April 18, 2026. The copyright holder for this preprint (which was not certified by peer review) is the author/funder. Creative Commons license: CC Attribution-NonCommercial-NoDerivatives 4.0 https://creativecommons.org/licenses/by-nc-nd/4.0

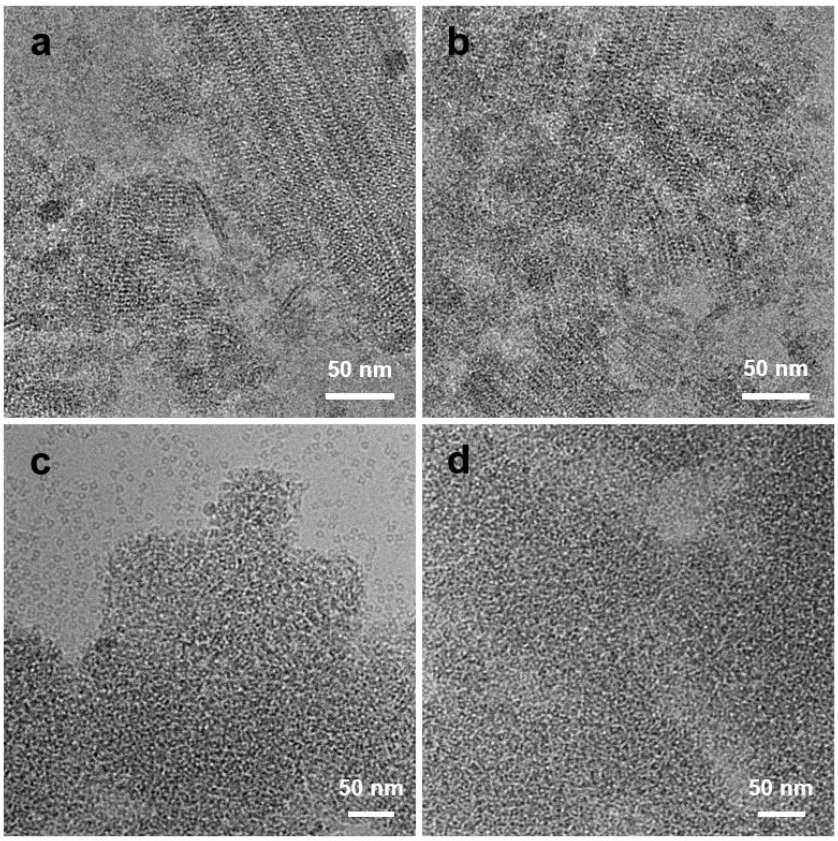

Supplementary Figure 6: Assembly formation and precipitation of purified UOX

a-b, Representative electron micrographs showing high-order assembly of purified UOX *in vitro*. Scale bars, 50 nm.

c-d, Representative electron micrographs showing precipitation of purified UOX *in vitro*. Scale bars, 50 nm.

Langtaosha (LTS) Preprint doi: https://doi.org/10.65215/LTSpreprints.2026.04.18.000189. This version posted April 18, 2026. The copyright holder for this preprint (which was not certified by peer review) is the author/funder. Creative Commons license: CC Attribution-NonCommercial-NoDerivatives 4.0 https://creativecommons.org/licenses/by-nc-nd/4.0

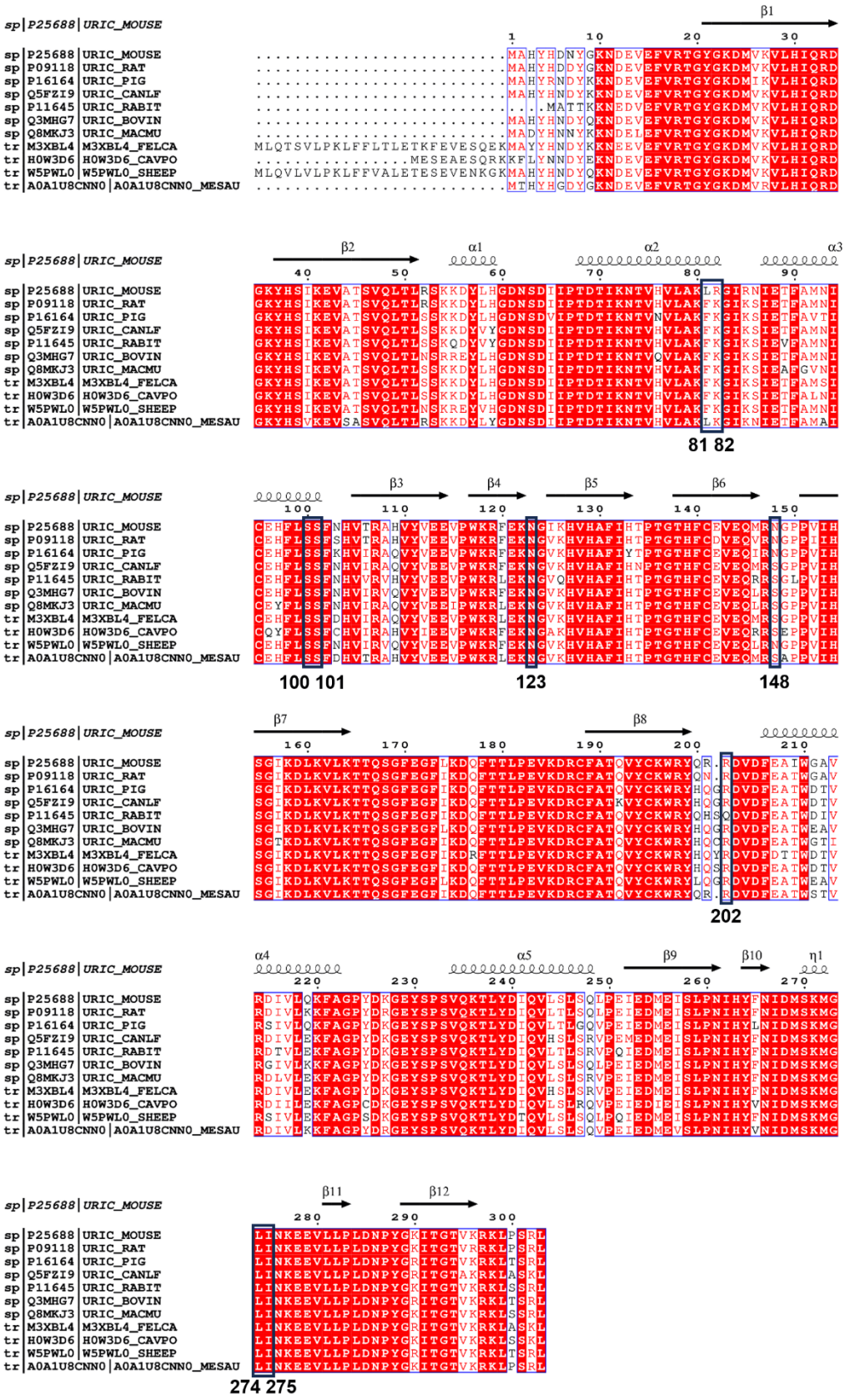

Supplementary Figure 7: Sequence alignment of UOX from mammals that has been reported the presence of putative UOX-derived crystalloid inclusions.

Langtaosha (LTS) Preprint doi: https://doi.org/10.65215/LTSpreprints.2026.04.18.000189. This version posted April 18, 2026. The copyright holder for this preprint (which was not certified by peer review) is the author/funder. Creative Commons license: CC Attribution-NonCommercial-NoDerivatives 4.0 https://creativecommons.org/licenses/by-nc-nd/4.0

UOX protein sequences from mouse (UniProt ID: P25688), rat (UniProt ID: P09118), pig (UniProt ID: P16164), dog (UniProt ID: Q5FZI9), rabbit (UniProt ID: P11645), bovine (UniProt ID: Q3MHG7), macaque (UniProt ID: Q8MKJ3), cat (UniProt ID: M3XBL4), guinea pig (UniProt ID: H0W3D6), sheep (UniProt ID: W5PWL0), hamster (UniProt ID: A0A1U8CNN0) were aligned using CLUSTALW [129]. The result was visualized with ESPript 3.0 [130], with key residues directly involved in UOX assembly formation highlighted in black frames.

Langtaosha (LTS) Preprint doi: https://doi.org/10.65215/LTSpreprints.2026.04.18.000189. This version posted April 18, 2026. The copyright holder for this preprint (which was not certified by peer review) is the author/funder. Creative Commons license: CC Attribution-NonCommercial-NoDerivatives 4.0 https://creativecommons.org/licenses/by-nc-nd/4.0

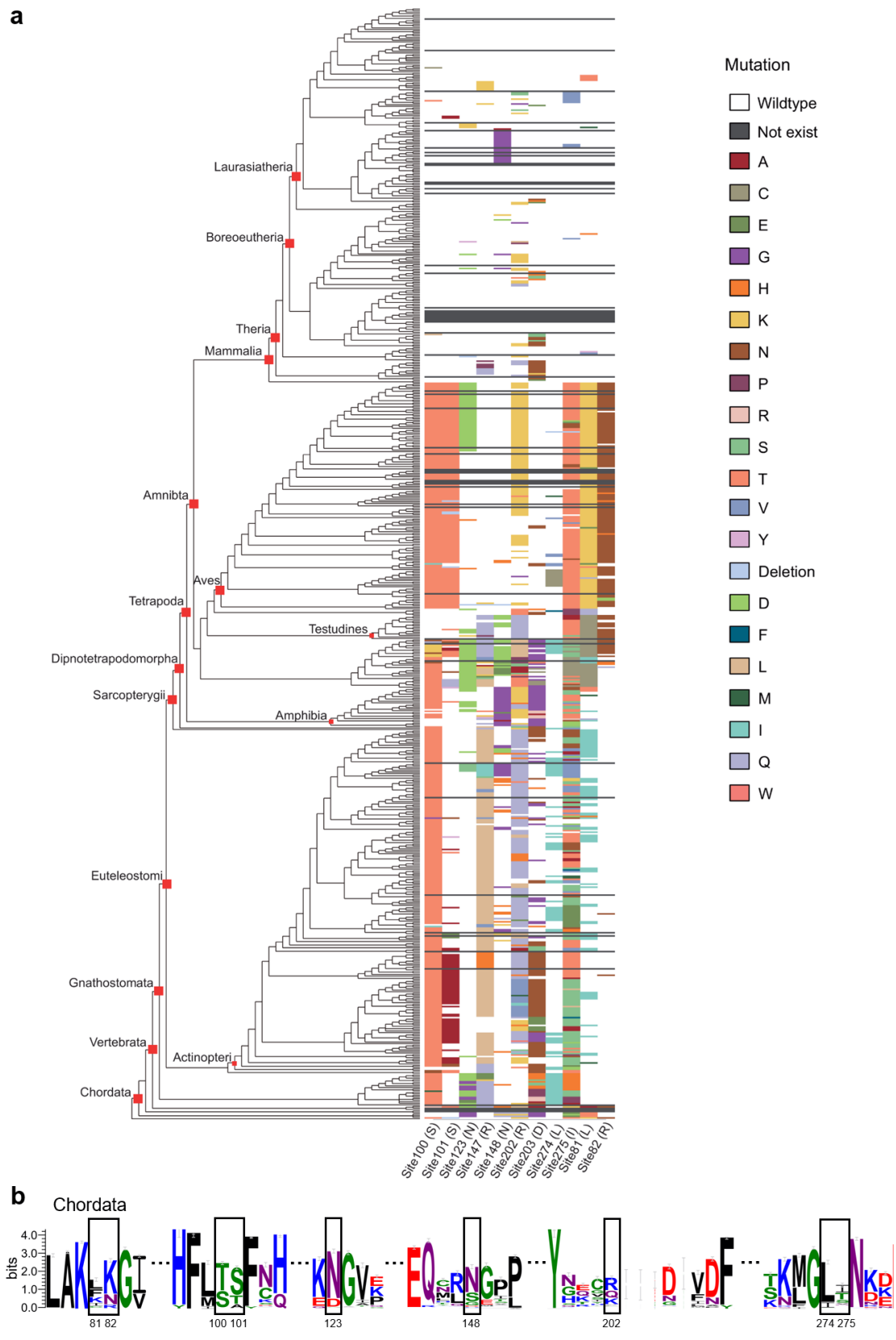

Supplementary Figure 8: The phylogenetic tree of UOX and mutation patterns of key UOX assembly-related residues across chordates.

a, Phylogenetic tree of UOX in Chordata and amino acid substitutions at 11 positions

Langtaosha (LTS) Preprint doi: https://doi.org/10.65215/LTSpreprints.2026.04.18.000189. This version posted April 18, 2026. The copyright holder for this preprint (which was not certified by peer review) is the author/funder. Creative Commons license: CC Attribution-NonCommercial-NoDerivatives 4.0 https://creativecommons.org/licenses/by-nc-nd/4.0

(100, 101, 123, 147, 148, 202, 203, 274, 275, 81, 82) that are closely associated with the assembly-forming of UOX. Each column represents one key residue, and each row represents a species. Different colors indicate different types of amino acid substitutions; white denotes no mutation at the corresponding position, and black indicates that the UOX sequence could not be identified in that species, suggesting a possible gene loss. Substitutions known and inferred not to affect assembly formation (L81F, R82K, N148S, R202Q) were excluded. Each position is annotated with the corresponding wild-type amino acid. Major evolutionary clades—such as Mammalia, Amniota, and Tetrapoda—are labeled alongside the phylogenetic tree.

b, Sequence conservation analysis of specific UOX motifs in Mammalia (n = 313), generated with WebLogo3 [70]. Residues directly involved in interactions are boxed in black. Numbers indicate corresponding residue positions in mouse UOX (UniProt ID: P25688).

Langtaosha (LTS) Preprint doi: https://doi.org/10.65215/LTSpreprints.2026.04.18.000189. This version posted April 18, 2026. The copyright holder for this preprint (which was not certified by peer review) is the author/funder. Creative Commons license: CC Attribution-NonCommercial-NoDerivatives 4.0 https://creativecommons.org/licenses/by-nc-nd/4.0

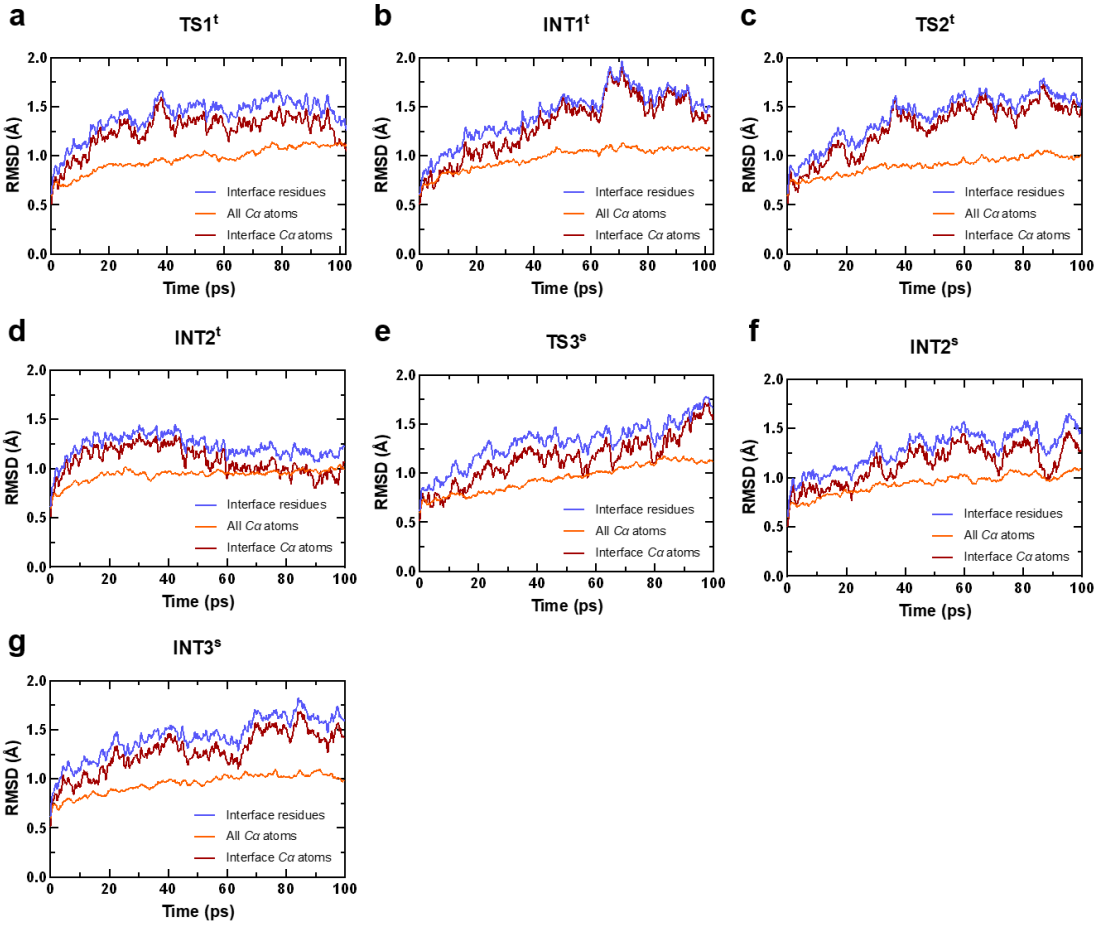

Supplementary Figure 9: Quantum mechanics/molecular mechanics simulation for UOX catalysis.

a-g, RMSD plot of UOX in complex with its substrate UA during the simulation of several reported transition states (TS) and intermediate states (INT) [124], using the MD-equilibrated structure as the reference. The superscript "t" represents triplet, and the superscript "s" represents singlet.

Langtaosha (LTS) Preprint doi: https://doi.org/10.65215/LTSpreprints.2026.04.18.000189. This version posted April 18, 2026. The copyright holder for this preprint (which was not certified by peer review) is the author/funder. Creative Commons license: CC Attribution-NonCommercial-NoDerivatives 4.0 https://creativecommons.org/licenses/by-nc-nd/4.0

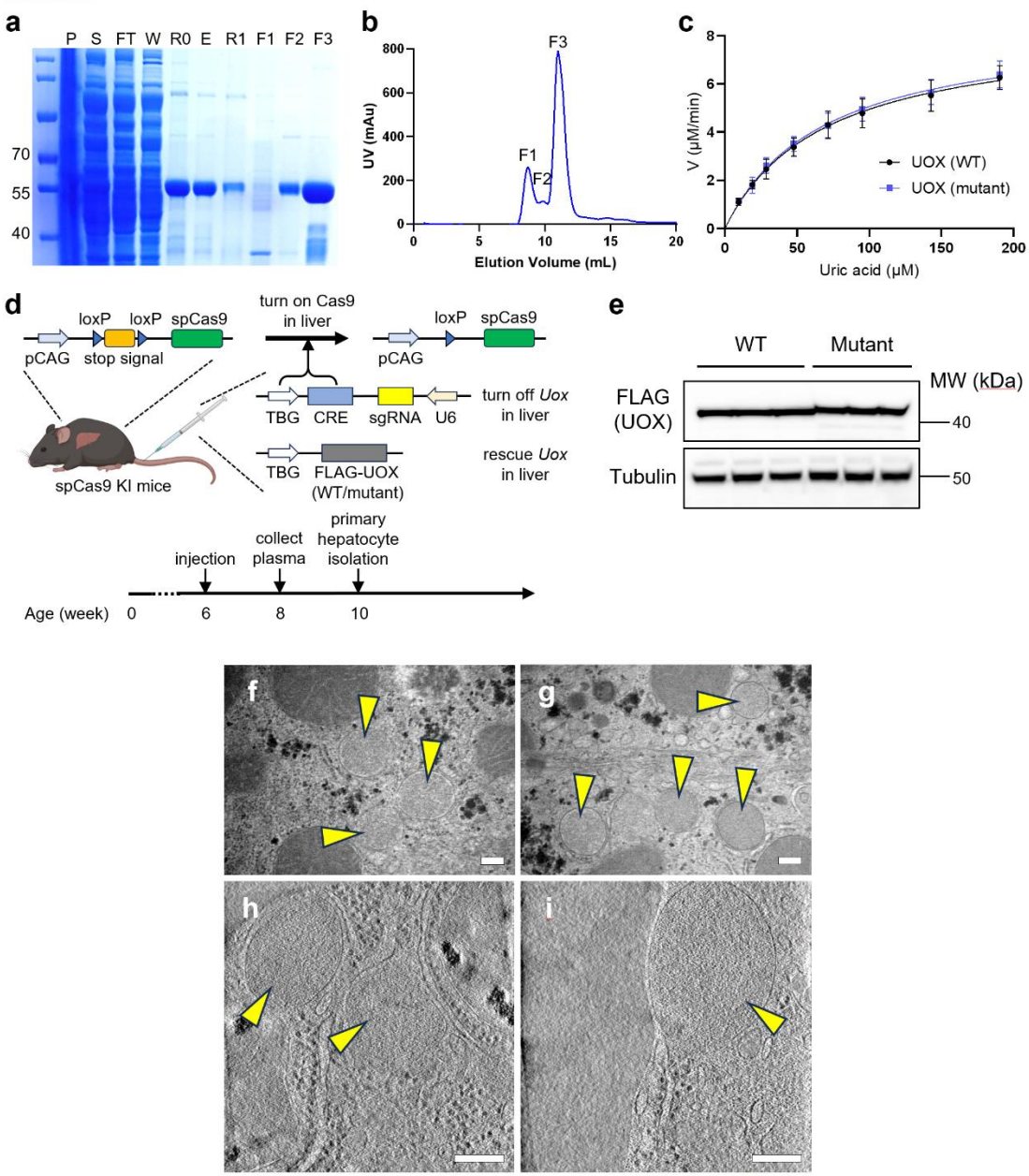

Supplementary Figure 10: Mutant UOX maintained normal tetramer formation and catalytic activity while completely abolishing high-order assembly.

a, SDS-PAGE with Coomassie Blue staining. Fraction1-3 (F1-F3) correspond to size exclusion chromatography fractions shown in (**b**). P, precipitation. S, supernatant. FT, flowthrough. W, wash. R0, resin before elution. E, eluate. R1, resin after elution.

b, Size exclusion chromatogram profile (Superdex 200 Increase 10/300 GL) of mutant UOX in the apo state.

c, Enzyme kinetics of wild-type UOX and mutant UOX. The rate (specific activity) of UA oxidation was measured by the linear decrease in absorbance at 293 nm. The data

Langtaosha (LTS) Preprint doi: https://doi.org/10.65215/LTSpreprints.2026.04.18.000189. This version posted April 18, 2026. The copyright holder for this preprint (which was not certified by peer review) is the author/funder. Creative Commons license: CC Attribution-NonCommercial-NoDerivatives 4.0 https://creativecommons.org/licenses/by-nc-nd/4.0

were fitted to the Michaelis-Menten equation by GraphPad Prism 9 to determine the k_{cat} and K_m values. The data are presented as the mean ± SD of at least three independent experiments.

d, Schematic of CRISPR–Cas9-mediated liver-specific knockout and rescue strategy in mice. The timeline illustrates key steps: AAV (Adeno-Associated Virus) injection, serum collection, and primary hepatocyte isolation.

e, Western blot analysis of FLAG-UOX and tubulin (loading control) in liver extracts from wild-type and UOX rescue mice.

f-g, Representative TEM images of liver from mutant UOX rescue mice. Yellow arrowheads indicate peroxisomes lacking UOX assembly. Scale bars, 200 nm.

h-i, Representative tomograms acquired from high-pressure frozen livers of mutant UOX rescue mice. Yellow arrowheads indicate peroxisomes lacking UOX assembly. Scale bars, 100 nm.

Langtaosha (LTS) Preprint doi: https://doi.org/10.65215/LTSpreprints.2026.04.18.000189. This version posted April 18, 2026. The copyright holder for this preprint (which was not certified by peer review) is the author/funder. Creative Commons license: CC Attribution-NonCommercial-NoDerivatives 4.0 https://creativecommons.org/licenses/by-nc-nd/4.0

Supplementary Table 1: Cryo-ET and cryo-EM data, map and atomic model statistics

	UOX fiber *in situ* (EMD-68844)	**UOX fiber *ex vivo* (EMD-68841) (PDB 23BU)**	**UOX homotetramers (apo) (EMD-68839) (PDB 23BS)**	**UOX homotetramers (urate bound) (EMD-68840) (PDB 23BT)**
Data collection and processing				
Magnification	64,000×	130,000×	165,000×	165,000×
Voltage (kV)	300	200	300	300
Electron exposure (e/Å^2)	110	60	60	60
Defocus range (μm)	-4.0 to -6.0	-1.0 to -2.0	-1.0 to -1.4	-1.0 to -1.4
Pixel size (Å)	1.37	0.93	0.74	0.74
Symmetry imposed	Helix	Helix, D1	D2	D2
Initial particle images (no.)	25,040	324,169	3,074,690	2,374,447
Final particle images (no.)	17,221 (22 tomograms)	219,322	101,075	304,325
Map resolution (Å)	7.3	3.64	2.79	2.42
FSC threshold	0.143	0.143	0.143	0.143
Map resolution range (Å)	6.5-11.1	3.4-3.7	2.8-3.3	2.2-2.8
Refinement				
Initial model used		AlphaFold2	AlphaFold2	AlphaFold2
Model resolution (Å)		3.7	2.8	2.4
FSC threshold		0.143	0.143	0.143
Model resolution range (Å)			2.8-3.2	2.4-2.7
Map sharpening *B* factor (Å^2)		-127.9	-28.1794	-102.2
Model composition				
Non-hydrogen atoms		9344	9276	9324
Protein residues		1148	1140	1140
Ligands		URC: 4	-	URC: 4
B factors (Å^2)				
Protein		77.26	127.4	47.59
Ligand		39.53	-	39.53

Langtaosha (LTS) Preprint doi: https://doi.org/10.65215/LTSpreprints.2026.04.18.000189. This version posted April 18, 2026. The copyright holder for this preprint (which was not certified by peer review) is the author/funder. Creative Commons license: CC Attribution-NonCommercial-NoDerivatives 4.0 https://creativecommons.org/licenses/by-nc-nd/4.0

R.m.s. deviations			
Bond lengths (Å)	0.003	0.003	0.004
Bond angles (°)	0.748	0.541	0.59
Validation			
MolProbity score	2.05	1.65	1.42
Clashscore	8.34	6.67	5.04
Poor rotamers (%)	3.07	0.00	0.00
Ramachandran plot			
Favored (%)	96.49	95.94	97.17
Allowed (%)	3.51	4.06	2.83
Disallowed (%)	0.00	0.00	0.00

Langtaosha (LTS) Preprint doi: https://doi.org/10.65215/LTSpreprints.2026.04.18.000189. This version posted April 18, 2026. The copyright holder for this preprint (which was not certified by peer review) is the author/funder. Creative Commons license: CC Attribution-NonCommercial-NoDerivatives 4.0 https://creativecommons.org/licenses/by-nc-nd/4.0

Supplementary Table S2: List of frequently detected mouse peroxisomal proteins (high detection frequency) and their Q-scores (Top12) by DiffFit

Langtaosha (LTS) Preprint doi: https://doi.org/10.65215/LTSpreprints.2026.04.18.000189. This version posted April 18, 2026. The copyright holder for this preprint (which was not certified by peer review) is the author/funder. Creative Commons license: CC Attribution-NonCommercial-NoDerivatives 4.0 https://creativecommons.org/licenses/by-nc-nd/4.0

Supplementary Table S3: The amino acid sequence of assembly-disrupting mutant *Mus musculus* UOX used in this study (The replaced sequences compared to WT UOX are colored in red)

Protein	Amino acid sequence
UOX (mutant)	MAHYHDNYGKNDEVEFVRTGYGKDMVKVLHIQRDGKYHSIKEVAT SVQLTLRSKKDYLHGDNSDIIPTDTIKNTVHVLAKLRGIRNIETFAMN ICEHFLSSFNHVTRAHVYVEEVPWKRFEKNGIKHVHAFIHTPTGTHF CEVEQMRNGPPVIHSGIKDLKVLKTTQSGFEGFLKDQFTTLPEVKDR CFATQVYCKWRYKNFSGLQEVRSHVPKFEAIWGAVRDIVLQKFAGP YDKGEYSPSVQKTLYDIQVLSLSQLPEIEDMEISLPNIHYFNIDMSKM GLINKEEVLLPLDNPYGKITGTVKRKLPSRL

Langtaosha (LTS) Preprint doi: https://doi.org/10.65215/LTSpreprints.2026.04.18.000189. This version posted April 18, 2026. The copyright holder for this preprint (which was not certified by peer review) is the author/funder. Creative Commons license: CC Attribution-NonCommercial-NoDerivatives 4.0 https://creativecommons.org/licenses/by-nc-nd/4.0

Supplementary Table S4: Enzyme kinetic parameters of wild-type and assembly disrupting mutant mouse UOX (Data are presented as mean ± SD across three independent assays)

	K_m (μM)	k_{cat} (s^{-1})	k_{cat}/K_m ($s^{-1} \cdot M^{-1}$)
UOX (WT)	69.7 ± 6.4	2.86 ± 0.25	(4.15 ± 0.69) × 10^4
UOX (mutant)	68.7 ± 7.7	2.97 ± 0.28	(4.36 ± 0.63) × 10^4

Langtaosha (LTS) Preprint doi: https://doi.org/10.65215/LTSpreprints.2026.04.18.000189. This version posted April 18, 2026. The copyright holder for this preprint (which was not certified by peer review) is the author/funder. Creative Commons license: CC Attribution-NonCommercial-NoDerivatives 4.0 https://creativecommons.org/licenses/by-nc-nd/4.0

Supplementary Video 1: The *in situ* structure of mouse UOX assembly in liver tissue

Langtaosha (LTS) Preprint doi: https://doi.org/10.65215/LTSpreprints.2026.04.18.000189. This version posted April 18, 2026. The copyright holder for this preprint (which was not certified by peer review) is the author/funder. Creative Commons license: CC Attribution-NonCommercial-NoDerivatives 4.0 https://creativecommons.org/licenses/by-nc-nd/4.0

References

1. Model, M.A., Hollembeak, J.E., and Kurokawa, M. (2021). Macromolecular Crowding: a Hidden Link Between Cell Volume and Everything Else. Cellular Physiology and Biochemistry: International Journal of Experimental Cellular Physiology, Biochemistry, and Pharmacology *55*, 25-40. 10.33594/000000319.
2. Rivas, G., and Minton, A.P. (2016). Macromolecular Crowding In Vitro, In Vivo, and In Between. Trends in Biochemical Sciences *41*, 970-981. 10.1016/j.tibs.2016.08.013.
3. Clegg, J.S. (1984). Properties and metabolism of the aqueous cytoplasm and its boundaries. The American Journal of Physiology *246*, R133-151. 10.1152/ajpregu.1984.246.2.R133.
4. Kim, Y.C., Best, R.B., and Mittal, J. (2010). Macromolecular crowding effects on protein-protein binding affinity and specificity. The Journal of Chemical Physics *133*, 205101. 10.1063/1.3516589.
5. McGuffee, S.R., and Elcock, A.H. (2010). Diffusion, crowding & protein stability in a dynamic molecular model of the bacterial cytoplasm. PLoS computational biology *6*, e1000694. 10.1371/journal.pcbi.1000694.
6. Huang, J.-H., and Ferrell, J.E., Jr. (2026). How does cytoplasmic crowding affect reaction rates? Molecular Cell. 10.1016/j.molcel.2025.12.007.
7. Alfano, C., Fichou, Y., Huber, K., Weiss, M., Spruijt, E., Ebbinghaus, S., De Luca, G., Morando, M.A., Vetri, V., Temussi, P.A., and Pastore, A. (2024). Molecular Crowding: The History and Development of a Scientific Paradigm. Chemical Reviews *124*, 3186-3219. 10.1021/acs.chemrev.3c00615.
8. Li, P., Banjade, S., Cheng, H.-C., Kim, S., Chen, B., Guo, L., Llaguno, M., Hollingsworth, J.V., King, D.S., Banani, S.F., et al. (2012). Phase transitions in the assembly of multivalent signalling proteins. Nature *483*, 336-340. 10.1038/nature10879.
9. Brangwynne, C.P., Eckmann, C.R., Courson, D.S., Rybarska, A., Hoege, C., Gharakhani, J., Jülicher, F., and Hyman, A.A. (2009). Germline P Granules Are Liquid Droplets That Localize by Controlled Dissolution/Condensation. Science *324*, 1729-1732. doi:10.1126/science.1172046.
10. Lafontaine, D.L.J., Riback, J.A., Bascetin, R., and Brangwynne, C.P. (2021). The nucleolus as a multiphase liquid condensate. Nature Reviews. Molecular Cell Biology *22*, 165-182. 10.1038/s41580-020-0272-6.
11. Protter, D.S.W., and Parker, R. (2016). Principles and Properties of Stress Granules. Trends in Cell Biology *26*, 668-679. 10.1016/j.tcb.2016.05.004.
12. Munishkina, L.A., Ahmad, A., Fink, A.L., and Uversky, V.N. (2008). Guiding protein aggregation with macromolecular crowding. Biochemistry *47*, 8993-9006. 10.1021/bi8008399.
13. Schönherr, R., Rudolph, J.M., and Redecke, L. (2018). Protein crystallization in living cells. Biological Chemistry *399*, 751-772. doi:10.1515/hsz-2018-0158.
14. Wu, Y., Qin, C., Du, W., Guo, Z., Chen, L., and Guo, Q. (2023). A practical multicellular sample preparation pipeline broadens the application of in situ cryo-electron tomography. Journal of Structural Biology *215*, 107971. 10.1016/j.jsb.2023.107971.
15. Tang, X., Qu, L., Wilfling, F., Beck, F., Ernst, O.P., Schulman, B.A., Baumeister, W., and Enenkel, C. Metabolically regulated proteasome supramolecular organization in

Langtaosha (LTS) Preprint doi: https://doi.org/10.65215/LTSpreprints.2026.04.18.000189. This version posted April 18, 2026. The copyright holder for this preprint (which was not certified by peer review) is the author/funder. Creative Commons license: CC Attribution-NonCommercial-NoDerivatives 4.0 https://creativecommons.org/licenses/by-nc-nd/4.0

situ. Cell. 10.1016/j.cell.2025.12.035.

16. Hyman, A.A., Weber, C.A., and Jülicher, F. (2014). Liquid-Liquid Phase Separation in Biology. Annual Review of Cell and Developmental Biology *30*, 39-58. https://doi.org/10.1146/annurev-cellbio-100913-013325.

17. Castellana, M., Wilson, M.Z., Xu, Y., Joshi, P., Cristea, I.M., Rabinowitz, J.D., Gitai, Z., and Wingreen, N.S. (2014). Enzyme clustering accelerates processing of intermediates through metabolic channeling. Nature Biotechnology *32*, 1011-1018. 10.1038/nbt.3018.

18. Liu, J.-L. (2016). The Cytoophidium and Its Kind: Filamentation and Compartmentation of Metabolic Enzymes. Annual Review of Cell and Developmental Biology *32*, 349-372. 10.1146/annurev-cellbio-111315-124907.

19. Petrovska, I., Nüske, E., Munder, M.C., Kulasegaran, G., Malinovska, L., Kroschwald, S., Richter, D., Fahmy, K., Gibson, K., Verbavatz, J.-M., and Alberti, S. (2014). Filament formation by metabolic enzymes is a specific adaptation to an advanced state of cellular starvation. eLife *3*, e02409. 10.7554/eLife.02409.

20. Labesse, G., Alexandre, T., Vaupré, L., Salard-Arnaud, I., Him, Joséphine Lai K., Raynal, B., Bron, P., and Munier-Lehmann, H. (2013). MgATP Regulates Allostery and Fiber Formation in IMPDHs. Structure *21*, 975-985. 10.1016/j.str.2013.03.011.

21. Sendker, F.L., Lo, Y.K., Heimerl, T., Bohn, S., Persson, L.J., Mais, C.-N., Sadowska, W., Paczia, N., Nußbaum, E., del Carmen Sánchez Olmos, M., et al. (2024). Emergence of fractal geometries in the evolution of a metabolic enzyme. Nature, 1-7. 10.1038/s41586-024-07287-2.

22. Bauerlein, F.J.B., and Baumeister, W. (2021). Towards Visual Proteomics at High Resolution. J Mol Biol *433*, 167187. 10.1016/j.jmb.2021.167187.

23. Parlakgül, G., Arruda, A.P., Pang, S., Cagampan, E., Min, N., Güney, E., Lee, G.Y., Inouye, K., Hess, H.F., Xu, C.S., and Hotamışlıgil, G.S. (2022). Regulation of liver subcellular architecture controls metabolic homeostasis. Nature *603*, 736-742. 10.1038/s41586-022-04488-5.

24. Ilacqua, N., Anastasia, I., Raimondi, A., Lemieux, P., De Aguiar Vallim, T.Q., Toth, K., Koonin, E.V., and Pellegrini, L. (2022). A three-organelle complex made by wrappER contacts with peroxisomes and mitochondria responds to liver lipid flux changes. Journal of Cell Science *135*. 10.1242/jcs.259091.

25. Bernhard, W., and Rouiller, C. (1956). Microbodies and the problem of mitochondrial regeneration in liver cells. The Journal of Biophysical and Biochemical Cytology *2*, 355-360. 10.1083/jcb.2.4.355.

26. De Duve, C., and Baudhuin, P. (1966). Peroxisomes (microbodies and related particles). Physiological Reviews *46*, 323-357. 10.1152/physrev.1966.46.2.323.

27. Gansler, H.d., and Rouiller, C. (2010). Modifications physiologiques et pathologiques du chondriome (Part 4 of 4): Etude au microscope électronique. Schweizerische Zeitschrift für allgemeine Pathologie und Bakteriologie *19*, 238-243. 10.1159/000317715.

28. Shnitka, T.K. (1966). Comparative ultrastructure of hepatic microbodies in some mammals and birds in relation to species differences in uricase activity. Journal of Ultrastructure Research *16*, 598-625. https://doi.org/10.1016/S0022-5320(66)80009-6.

29. Hruban, Z., and Swift, H. (1964). URICASE: LOCALIZATION IN HEPATIC MICROBODIES. Science (New York, N.Y.) *146*, 1316-1318. 10.1126/science.146.3649.1316.

Langtaosha (LTS) Preprint doi: https://doi.org/10.65215/LTSpreprints.2026.04.18.000189. This version posted April 18, 2026. The copyright holder for this preprint (which was not certified by peer review) is the author/funder. Creative Commons license: CC Attribution-NonCommercial-NoDerivatives 4.0 https://creativecommons.org/licenses/by-nc-nd/4.0

30. Tsukada, H., Mochizuki, Y., and Fujiwara, S. (1966). The nucleoids of rat liver cell microbodies. Fine structure and enzymes. The Journal of Cell Biology *28*, 449-460. 10.1083/jcb.28.3.449.

31. Jumper, J., Evans, R., Pritzel, A., Green, T., Figurnov, M., Ronneberger, O., Tunyasuvunakool, K., Bates, R., Žídek, A., Potapenko, A., et al. (2021). Highly accurate protein structure prediction with AlphaFold. Nature *596*, 583-589. 10.1038/s41586-021-03819-2.

32. Yifrach, E., Fischer, S., Oeljeklaus, S., Schuldiner, M., Zalckvar, E., and Warscheid, B. (2018). Defining the Mammalian Peroxisomal Proteome. Sub-Cellular Biochemistry *89*, 47-66. 10.1007/978-981-13-2233-4_2.

33. Luo, D., Alsuwaykit, Z., Khan, D., Strnad, O., Isenberg, T., and Viola, I. (2025). DiffFit: Visually-Guided Differentiable Fitting of Molecule Structures to a Cryo-EM Map. IEEE Transactions on Visualization and Computer Graphics *31*, 558-568. 10.1109/TVCG.2024.3456404.

34. Pintilie, G., Zhang, K., Su, Z., Li, S., Schmid, M.F., and Chiu, W. (2020). Measurement of atom resolvability in cryo-EM maps with Q-scores. Nature Methods *17*, 328-334. 10.1038/s41592-020-0731-1.

35. Kahn, K., Serfozo, P., and Tipton, P.A. (1997). Identification of the True Product of the Urate Oxidase Reaction. Journal of the American Chemical Society *119*, 5435-5442. 10.1021/ja970375t.

36. Modrić, N., Derome, A.E., Ashcroft, S.J.H., and Poje, M. (1992). Tracing and identification of uricase. Reaction intermediates.: A direct 13C-NMR/isotope-labelling evidence. Tetrahedron Letters *33*, 6691-6694. 10.1016/S0040-4039(00)61021-3.

37. Völkl, A., Baumgart, E., and Fahimi, H.D. (1988). Localization of urate oxidase in the crystalline cores of rat liver peroxisomes by immunocytochemistry and immunoblotting. Journal of Histochemistry & Cytochemistry *36*, 329-336. 10.1177/36.4.3346536.

38. Usuda, N., Reddy, M.K., Hashimoto, T., Rao, M.S., and Reddy, J.K. (1988). Tissue specificity and species differences in the distribution of urate oxidase in peroxisomes. Laboratory Investigation; a Journal of Technical Methods and Pathology *58*, 100-111.

39. Angermüller, S., and Fahimi, H.D. (1986). Ultrastructural cytochemical localization of uricase in peroxisomes of rat liver. Journal of Histochemistry & Cytochemistry *34*, 159-165. 10.1177/34.2.3080517.

40. Leighton, F., Poole, B., Lazarow, P.B., and De Duve, C. (1969). THE SYNTHESIS AND TURNOVER OF RAT LIVER PEROXISOMES : I. Fractionation of Peroxisome Proteins. Journal of Cell Biology *41*, 521-535. 10.1083/jcb.41.2.521.

41. Wang, C., Jiang, W., Leitz, J., Yang, K., Esquivies, L., Wang, X., Shen, X., Held, R.G., Adams, D.J., Basta, T., et al. (2024). Structure and topography of the synaptic V-ATPase–synaptophysin complex. Nature, 1-6. 10.1038/s41586-024-07610-x.

42. Zheng, W., Chai, P., Zhu, J., and Zhang, K. (2024). High-resolution in situ structures of mammalian respiratory supercomplexes. Nature, 1-8. 10.1038/s41586-024-07488-9.

43. Friedman, T.B., Polanco, G.E., Appold, J.C., and Mayle, J.E. (1985). On the loss of uricolytic activity during primate evolution—I. Silencing of urate oxidase in a hominoid ancestor. Comparative Biochemistry and Physiology Part B: Comparative Biochemistry *81*, 653-659. https://doi.org/10.1016/0305-0491(85)90381-5.

44. Fujiwara, S., Ohashi, H., and Noguchi, T. (1987). Comparison of intraperoxisomal

Langtaosha (LTS) Preprint doi: https://doi.org/10.65215/LTSpreprints.2026.04.18.000189. This version posted April 18, 2026. The copyright holder for this preprint (which was not certified by peer review) is the author/funder. Creative Commons license: CC Attribution-NonCommercial-NoDerivatives 4.0 https://creativecommons.org/licenses/by-nc-nd/4.0

localization form and properties of amphibian (Rana catesbeiana) uricase with those of other animal uricases. Comparative Biochemistry and Physiology. B, Comparative Biochemistry *86*, 23-26. 10.1016/0305-0491(87)90169-6.

45. Noguchi, T., Takada, Y., and Fujiwara, S. (1979). Degradation of uric acid to urea and glyoxylate in peroxisomes. Journal of Biological Chemistry *254*, 5272-5275. 10.1016/S0021-9258(18)50590-1.

46. Fujiwara, S., Nakashima, K., and Noguchi, T. (1987). Insoluble uricase in liver peroxisomes of Old World monkeys. Comparative Biochemistry and Physiology. B, Comparative Biochemistry *88*, 467-469. 10.1016/0305-0491(87)90328-2.

47. Feng, S., Aplin, C., Nguyen, T.-T.T., Milano, S.K., and Cerione, R.A. (2024). Filament formation drives catalysis by glutaminase enzymes important in cancer progression. Nature Communications *15*, 1971. 10.1038/s41467-024-46351-3.

48. Hvorecny, K.L., Hargett, K., Quispe, J.D., and Kollman, J.M. (2023). Human PRPS1 filaments stabilize allosteric sites to regulate activity. Nature Structural & Molecular Biology *30*, 391-402. 10.1038/s41594-023-00921-z.

49. Colloc'h, N., el Hajji, M., Bachet, B., L'Hermite, G., Schiltz, M., Prangé, T., Castro, B., and Mornon, J.P. (1997). Crystal structure of the protein drug urate oxidase-inhibitor complex at 2.05 A resolution. Nature Structural Biology *4*, 947-952. 10.1038/nsb1197-947.

50. Davies, Michael J. (2016). Protein oxidation and peroxidation. Biochemical Journal *473*, 805-825. 10.1042/bj20151227.

51. Celi, P., and Gabai, G. (2015). Oxidant/Antioxidant Balance in Animal Nutrition and Health: The Role of Protein Oxidation. Frontiers in Veterinary Science *2*. 10.3389/fvets.2015.00048.

52. Davies, M.J. (2005). The oxidative environment and protein damage. Biochimica et Biophysica Acta (BBA) - Proteins and Proteomics *1703*, 93-109. 10.1016/j.bbapap.2004.08.007.

53. Garcia-Seisdedos, H., Empereur-Mot, C., Elad, N., and Levy, E.D. (2017). Proteins evolve on the edge of supramolecular self-assembly. Nature *548*, 244-247. 10.1038/nature23320.

54. Pillai, A.S., Chandler, S.A., Liu, Y., Signore, A.V., Cortez-Romero, C.R., Benesch, J.L.P., Laganowsky, A., Storz, J.F., Hochberg, G.K.A., and Thornton, J.W. (2020). Origin of complexity in haemoglobin evolution. Nature *581*, 480-485. 10.1038/s41586-020-2292-y.

55. Grueninger, D., Treiber, N., Ziegler, M.O.P., Koetter, J.W.A., Schulze, M.-S., and Schulz, G.E. (2008). Designed Protein-Protein Association. Science *319*, 206-209. doi:10.1126/science.1150421.

56. Hvorecny, K.L., and Kollman, J.M. (2023). Greater than the sum of parts: Mechanisms of metabolic regulation by enzyme filaments. Current Opinion in Structural Biology *79*, 102530. https://doi.org/10.1016/j.sbi.2023.102530.

57. Park, C.K., and Horton, N.C. (2019). Structures, functions, and mechanisms of filament forming enzymes: a renaissance of enzyme filamentation. Biophysical Reviews *11*, 927-994. 10.1007/s12551-019-00602-6.

58. Ramazzina, I., Folli, C., Secchi, A., Berni, R., and Percudani, R. (2006). Completing the uric acid degradation pathway through phylogenetic comparison of whole genomes. Nature Chemical Biology *2*, 144-148. 10.1038/nchembio768.

59. Sarma, A.D., Serfozo, P., Kahn, K., and Tipton, P.A. (1999). Identification and Purification of

Langtaosha (LTS) Preprint doi: https://doi.org/10.65215/LTSpreprints.2026.04.18.000189. This version posted April 18, 2026. The copyright holder for this preprint (which was not certified by peer review) is the author/funder. Creative Commons license: CC Attribution-NonCommercial-NoDerivatives 4.0 https://creativecommons.org/licenses/by-nc-nd/4.0

Hydroxyisourate Hydrolase, a Novel Ureide-metabolizing Enzyme*. Journal of Biological Chemistry *274*, 33863-33865. 10.1074/jbc.274.48.33863.

60. Schultz, A.C., Nygaard, P., and Saxild, H.H. (2001). Functional Analysis of 14 Genes That Constitute the Purine Catabolic Pathway in Bacillus subtilis and Evidence for a Novel Regulon Controlled by the PucR Transcription Activator. Journal of Bacteriology *183*, 3293-3302. 10.1128/jb.183.11.3293-3302.2001.

61. Sun, Z., Zhang, X., Zhao, Z., Li, X., Pang, J., and Chen, J. (2024). Recent Progress and Future Perspectives on Anti-Hyperuricemic Agents. Journal of Medicinal Chemistry. 10.1021/acs.jmedchem.4c01260.

62. Pui, C.-H. (2002). Rasburicase: a potent uricolytic agent. Expert Opinion on Pharmacotherapy *3*, 433-442. 10.1517/14656566.3.4.433.

63. Schlesinger, N., Yasothan, U., and Kirkpatrick, P. (2011). Pegloticase. Nature Reviews Drug Discovery *10*, 17-18. 10.1038/nrd3349.

64. Schlesinger, N., Pérez-Ruiz, F., and Lioté, F. (2023). Mechanisms and rationale for uricase use in patients with gout. Nature Reviews Rheumatology *19*, 640-649. 10.1038/s41584-023-01006-3.

65. Duan, Y., Jiang, N., Chen, J., and Chen, J. (2021). Expression, localization and metabolic function of "resurrected" human urate oxidase in human hepatocytes. International Journal of Biological Macromolecules *175*, 30-39. 10.1016/j.ijbiomac.2021.01.163.

66. Li, Z., Hoshino, Y., Tran, L., and Gaucher, E.A. (2022). Phylogenetic Articulation of Uric Acid Evolution in Mammals and How It Informs a Therapeutic Uricase. Molecular Biology and Evolution *39*, msab312. 10.1093/molbev/msab312.

67. Yang, B., Luo, G., Nie, T., Ban, Z., Ning, Q., Zhang, J., Liu, X., Lin, Y., Xie, X., Chen, Q., et al. (2025). Biomimetic bioreactor for potentiated uricase replacement therapy in hyperuricemia and gout. Frontiers in Bioengineering and Biotechnology *12*. 10.3389/fbioe.2024.1520663.

68. Tran, L., Das, S., Zhao, L., Finn, M.G., and Gaucher, E.A. (2023). Oral Delivery of Nanoparticles Carrying Ancestral Uricase Enzyme Protects against Hyperuricemia in Knockout Mice. Biomacromolecules *24*, 2003-2008. 10.1021/acs.biomac.2c01388.

69. Gong, X., Liu, S., Xia, B., Wan, Y., Zhang, S., Zhang, B., Wang, Z., Chen, J., Xiao, F., Liang, X.-J., and Yang, Y. (2025). Oral delivery of therapeutic proteins by engineered bacterial type zero secretion system. Nature Communications *16*, 1862. 10.1038/s41467-025-57153-6.

70. Crooks, G.E., Hon, G., Chandonia, J.-M., and Brenner, S.E. (2004). WebLogo: A Sequence Logo Generator: Figure 1. Genome Research *14*, 1188-1190. 10.1101/gr.849004.

71. Wenjing, D., Junhan, Y., and Qiang, G. (2025). Optimized Tissue Sample Preparation for Cryo-Electron Tomography Using Serial Lift-Out. Biophysics Reports *0*, 0. 10.52601/bpr.2025.250035.

72. Schiøtz, O.H., Kaiser, C.J.O., Klumpe, S., Morado, D.R., Poege, M., Schneider, J., Beck, F., Klebl, D.P., Thompson, C., and Plitzko, J.M. (2023). Serial Lift-Out: sampling the molecular anatomy of whole organisms. Nature Methods, 1-9. 10.1038/s41592-023-02113-5.

73. Mastronarde, D.N. (2005). Automated electron microscope tomography using robust prediction of specimen movements. Journal of Structural Biology *152*, 36-51. 10.1016/j.jsb.2005.07.007.

Langtaosha (LTS) Preprint doi: https://doi.org/10.65215/LTSpreprints.2026.04.18.000189. This version posted April 18, 2026. The copyright holder for this preprint (which was not certified by peer review) is the author/funder. Creative Commons license: CC Attribution-NonCommercial-NoDerivatives 4.0 https://creativecommons.org/licenses/by-nc-nd/4.0

74. Eisenstein, F., Yanagisawa, H., Kashihara, H., Kikkawa, M., Tsukita, S., and Danev, R. (2023). Parallel cryo electron tomography on in situ lamellae. Nature Methods *20*, 131-138. 10.1038/s41592-022-01690-1.

75. Turoňová, B., Hagen, W.J.H., Obr, M., Mosalaganti, S., Beugelink, J.W., Zimmerli, C.E., Kräusslich, H.-G., and Beck, M. (2020). Benchmarking tomographic acquisition schemes for high-resolution structural biology. Nature Communications *11*, 876. 10.1038/s41467-020-14535-2.

76. Hagen, W.J.H., Wan, W., and Briggs, J.A.G. (2017). Implementation of a cryo-electron tomography tilt-scheme optimized for high resolution subtomogram averaging. Journal of Structural Biology *197*, 191-198. 10.1016/j.jsb.2016.06.007.

77. Khavnekar, S., Erdmann, P.S., and Wan, W. (2024). TOMOMAN: a software package for large-scale cryo-electron tomography data preprocessing, community data sharing and collaborative computing. Journal of Applied Crystallography *57*, 2010-2016. 10.1107/S1600576724010264.

78. Nickell, S., Förster, F., Linaroudis, A., Net, W.D., Beck, F., Hegerl, R., Baumeister, W., and Plitzko, J.M. (2005). TOM software toolbox: acquisition and analysis for electron tomography. Journal of Structural Biology *149*, 227-234. 10.1016/j.jsb.2004.10.006.

79. Zheng, S.Q., Palovcak, E., Armache, J.-P., Verba, K.A., Cheng, Y., and Agard, D.A. (2017). MotionCor2: anisotropic correction of beam-induced motion for improved cryo-electron microscopy. Nature Methods *14*, 331-332. 10.1038/nmeth.4193.

80. Grant, T., and Grigorieff, N. (2015). Measuring the optimal exposure for single particle cryo-EM using a 2.6 Å reconstruction of rotavirus VP6. eLife *4*, e06980. 10.7554/eLife.06980.

81. Zheng, S., Wolff, G., Greenan, G., Chen, Z., Faas, F.G.A., Bárcena, M., Koster, A.J., Cheng, Y., and Agard, D.A. (2022). AreTomo: An integrated software package for automated marker-free, motion-corrected cryo-electron tomographic alignment and reconstruction. Journal of Structural Biology: X *6*, 100068. 10.1016/j.yjsbx.2022.100068.

82. Kremer, J.R., Mastronarde, D.N., and McIntosh, J.R. (1996). Computer Visualization of Three-Dimensional Image Data Using IMOD. Journal of Structural Biology *116*, 71-76. 10.1006/jsbi.1996.0013.

83. Buchholz, T.-O., Jordan, M., Pigino, G., and Jug, F. (2019). Cryo-CARE: Content-Aware Image Restoration for Cryo-Transmission Electron Microscopy Data. 2019 IEEE 16th International Symposium on Biomedical Imaging (ISBI 2019), 502-506. 10.1109/ISBI.2019.8759519.

84. Liu, Y.-T., Zhang, H., Wang, H., Tao, C.-L., Bi, G.-Q., and Zhou, Z.H. (2022). Isotropic reconstruction for electron tomography with deep learning. Nature Communications *13*, 6482. 10.1038/s41467-022-33957-8.

85. Tegunov, D., and Cramer, P. (2019). Real-time cryo-electron microscopy data preprocessing with Warp. Nature Methods *16*, 1146-1152. 10.1038/s41592-019-0580-y.

86. Scheres, S.H.W. (2012). RELION: Implementation of a Bayesian approach to cryo-EM structure determination. Journal of Structural Biology *180*, 519-530. 10.1016/j.jsb.2012.09.006.

87. Tegunov, D., Xue, L., Dienemann, C., Cramer, P., and Mahamid, J. (2021). Multi-particle cryo-EM refinement with M visualizes ribosome-antibiotic complex at 3.5 Å in cells.

Langtaosha (LTS) Preprint doi: https://doi.org/10.65215/LTSpreprints.2026.04.18.000189. This version posted April 18, 2026. The copyright holder for this preprint (which was not certified by peer review) is the author/funder. Creative Commons license: CC Attribution-NonCommercial-NoDerivatives 4.0 https://creativecommons.org/licenses/by-nc-nd/4.0

Nature Methods *18*, 186-193. 10.1038/s41592-020-01054-7.

88. Meng, E.C., Goddard, T.D., Pettersen, E.F., Couch, G.S., Pearson, Z.J., Morris, J.H., and Ferrin, T.E. (2023). UCSF ChimeraX: Tools for structure building and analysis. Protein Science *32*, e4792. 10.1002/pro.4792.

89. Kimanius, D., Forsberg, B.O., Scheres, S.H., and Lindahl, E. (2016). Accelerated cryo-EM structure determination with parallelisation using GPUs in RELION-2. eLife *5*, e18722. 10.7554/eLife.18722.

90. Zivanov, J., Nakane, T., Forsberg, B.O., Kimanius, D., Hagen, W.J., Lindahl, E., and Scheres, S.H. (2018). New tools for automated high-resolution cryo-EM structure determination in RELION-3. eLife *7*, e42166. 10.7554/eLife.42166.

91. Roth, P., Ermel, U.H., Moser, D., Arctaedius, G., Wehrheim, M., Scheffer, M.P., and Frangakis, A.S. (2025). ArtiaX: geometric models, camera paths and image processing tools. Journal of Structural Biology *217*, 108215. 10.1016/j.jsb.2025.108215.

92. He, S., and Scheres, S.H.W. (2017). Helical reconstruction in RELION. Journal of Structural Biology *198*, 163-176. 10.1016/j.jsb.2017.02.003.

93. Chaillet, M.L., van der Schot, G., Gubins, I., Roet, S., Veltkamp, R.C., and Förster, F. (2023). Extensive Angular Sampling Enables the Sensitive Localization of Macromolecules in Electron Tomograms. International Journal of Molecular Sciences *24*, 13375. 10.3390/ijms241713375.

94. Moebel, E., Martinez-Sanchez, A., Lamm, L., Righetto, R.D., Wietrzynski, W., Albert, S., Larivière, D., Fourmentin, E., Pfeffer, S., Ortiz, J., et al. (2021). Deep learning improves macromolecule identification in 3D cellular cryo-electron tomograms. Nature Methods *18*, 1386-1394. 10.1038/s41592-021-01275-4.

95. Lamm, L., Zufferey, S., Righetto, R.D., Wietrzynski, W., Yamauchi, K.A., Burt, A., Liu, Y., Zhang, H., Martinez-Sanchez, A., Ziegler, S., et al. (2024). MemBrain v2: an end-to-end tool for the analysis of membranes in cryo-electron tomography. 10.1101/2024.01.05.574336.

96. Manner, A., and Islinger, M. (2023). Isolation of Mammalian Peroxisomes by Density Gradient Centrifugation. In Peroxisomes: Methods and Protocols, M. Schrader, ed. (Springer US), pp. 1-12.

97. Manner, A., and Islinger, M. (2017). Isolation of Peroxisomes from Rat Liver and Cultured Hepatoma Cells by Density Gradient Centrifugation. In Peroxisomes: Methods and Protocols, M. Schrader, ed. (Springer), pp. 1-11.

98. Kimanius, D., Dong, L., Sharov, G., Nakane, T., and Scheres, S.H.W. (2021). New tools for automated cryo-EM single-particle analysis in RELION-4.0. The Biochemical Journal *478*, 4169-4185. 10.1042/BCJ20210708.

99. Rohou, A., and Grigorieff, N. (2015). CTFFIND4: Fast and accurate defocus estimation from electron micrographs. Journal of Structural Biology *192*, 216-221. 10.1016/j.jsb.2015.08.008.

100. Zivanov, J., Nakane, T., and Scheres, S.H.W. (2019). A Bayesian approach to beam-induced motion correction in cryo-EM single-particle analysis. IUCrJ *6*, 5-17. 10.1107/S205225251801463X.

101. Rosenthal, P.B., and Henderson, R. (2003). Optimal determination of particle orientation, absolute hand, and contrast loss in single-particle electron cryomicroscopy. Journal of

Langtaosha (LTS) Preprint doi: https://doi.org/10.65215/LTSpreprints.2026.04.18.000189. This version posted April 18, 2026. The copyright holder for this preprint (which was not certified by peer review) is the author/funder. Creative Commons license: CC Attribution-NonCommercial-NoDerivatives 4.0 https://creativecommons.org/licenses/by-nc-nd/4.0

Molecular Biology *333*, 721-745. 10.1016/j.jmb.2003.07.013.

102. Sanchez-Garcia, R., Gomez-Blanco, J., Cuervo, A., Carazo, J.M., Sorzano, C.O.S., and Vargas, J. (2021). DeepEMhancer: a deep learning solution for cryo-EM volume post-processing. Communications Biology *4*, 1-8. 10.1038/s42003-021-02399-1.

103. Tan, Y.Z., Baldwin, P.R., Davis, J.H., Williamson, J.R., Potter, C.S., Carragher, B., and Lyumkis, D. (2017). Addressing preferred specimen orientation in single-particle cryo-EM through tilting. Nature Methods *14*, 793-796. 10.1038/nmeth.4347.

104. Punjani, A., Rubinstein, J.L., Fleet, D.J., and Brubaker, M.A. (2017). cryoSPARC: algorithms for rapid unsupervised cryo-EM structure determination. Nature Methods *14*, 290-296. 10.1038/nmeth.4169.

105. Bepler, T., Morin, A., Rapp, M., Brasch, J., Shapiro, L., Noble, A.J., and Berger, B. (2019). Positive-unlabeled convolutional neural networks for particle picking in cryo-electron micrographs. Nature Methods *16*, 1153-1160. 10.1038/s41592-019-0575-8.

106. Punjani, A., Zhang, H., and Fleet, D.J. (2020). Non-uniform refinement: adaptive regularization improves single-particle cryo-EM reconstruction. Nature Methods *17*, 1214-1221. 10.1038/s41592-020-00990-8.

107. He, J., Li, T., and Huang, S.-Y. (2023). Improvement of cryo-EM maps by simultaneous local and non-local deep learning. Nature Communications *14*, 3217. 10.1038/s41467-023-39031-1.

108. Jamali, K., Käll, L., Zhang, R., Brown, A., Kimanius, D., and Scheres, S.H.W. (2024). Automated model building and protein identification in cryo-EM maps. Nature *628*, 450-457. 10.1038/s41586-024-07215-4.

109. Xu, K., Wang, Z., Shi, J., Li, H., and Zhang, Q.C. (2019). A^2-Net: Molecular Structure Estimation from Cryo-EM Density Volumes. 10.48550/arXiv.1901.00785.

110. Emsley, P., Lohkamp, B., Scott, W.G., and Cowtan, K. (2010). Features and development of Coot. Acta Crystallographica Section D: Biological Crystallography *66*, 486-501. 10.1107/S0907444910007493.

111. Afonine, P.V., Poon, B.K., Read, R.J., Sobolev, O.V., Terwilliger, T.C., Urzhumtsev, A., and Adams, P.D. (2018). Real-space refinement in PHENIX for cryo-EM and crystallography. Acta Crystallographica. Section D, Structural Biology *74*, 531-544. 10.1107/S2059798318006551.

112. Adams, P.D., Afonine, P.V., Bunkóczi, G., Chen, V.B., Davis, I.W., Echols, N., Headd, J.J., Hung, L.-W., Kapral, G.J., Grosse-Kunstleve, R.W., et al. (2010). PHENIX: a comprehensive Python-based system for macromolecular structure solution. Acta Crystallographica Section D: Biological Crystallography *66*, 213-221. 10.1107/S0907444909052925.

113. Williams, C.J., Headd, J.J., Moriarty, N.W., Prisant, M.G., Videau, L.L., Deis, L.N., Verma, V., Keedy, D.A., Hintze, B.J., Chen, V.B., et al. (2018). MolProbity: More and better reference data for improved all-atom structure validation. Protein Science: A Publication of the Protein Society *27*, 293-315. 10.1002/pro.3330.

114. Pettersen, E.F., Goddard, T.D., Huang, C.C., Couch, G.S., Greenblatt, D.M., Meng, E.C., and Ferrin, T.E. (2004). UCSF Chimera--a visualization system for exploratory research and analysis. Journal of Computational Chemistry *25*, 1605-1612. 10.1002/jcc.20084.

115. Schrödinger, L. (2015). The PyMOL Molecular Graphics System, Version 3.0.

116. Abramson, J., Adler, J., Dunger, J., Evans, R., Green, T., Pritzel, A., Ronneberger, O.,

Langtaosha (LTS) Preprint doi: https://doi.org/10.65215/LTSpreprints.2026.04.18.000189. This version posted April 18, 2026. The copyright holder for this preprint (which was not certified by peer review) is the author/funder. Creative Commons license: CC Attribution-NonCommercial-NoDerivatives 4.0 https://creativecommons.org/licenses/by-nc-nd/4.0

Willmore, L., Ballard, A.J., Bambrick, J., et al. (2024). Accurate structure prediction of biomolecular interactions with AlphaFold 3. Nature *630*, 493-500. 10.1038/s41586-024-07487-w.

117. Wang, X., Xu, B.-L., and Chen, X.-W. (2021). Acute gene inactivation in the adult mouse liver using the CRISPR-Cas9 technology. STAR Protocols *2*, 100611. 10.1016/j.xpro.2021.100611.

118. Weerapana, E., Wang, C., Simon, G.M., Richter, F., Khare, S., Dillon, M.B.D., Bachovchin, D.A., Mowen, K., Baker, D., and Cravatt, B.F. (2010). Quantitative reactivity profiling predicts functional cysteines in proteomes. Nature *468*, 790-795. 10.1038/nature09472.

119. Eastman, P., Swails, J., Chodera, J.D., McGibbon, R.T., Zhao, Y., Beauchamp, K.A., Wang, L.-P., Simmonett, A.C., Harrigan, M.P., Stern, C.D., et al. (2017). OpenMM 7: Rapid development of high performance algorithms for molecular dynamics. PLOS Computational Biology *13*, e1005659. 10.1371/journal.pcbi.1005659.

120. O'Boyle, N.M., Banck, M., James, C.A., Morley, C., Vandermeersch, T., and Hutchison, G.R. (2011). Open Babel: An open chemical toolbox. Journal of Cheminformatics *3*, 33. 10.1186/1758-2946-3-33.

121. Maier, J.A., Martinez, C., Kasavajhala, K., Wickstrom, L., Hauser, K.E., and Simmerling, C. (2015). ff14SB: Improving the Accuracy of Protein Side Chain and Backbone Parameters from ff99SB. Journal of Chemical Theory and Computation *11*, 3696-3713. 10.1021/acs.jctc.5b00255.

122. Jorgensen, W.L., Chandrasekhar, J., Madura, J.D., Impey, R.W., and Klein, M.L. (1983). Comparison of simple potential functions for simulating liquid water. The Journal of Chemical Physics *79*, 926-935. 10.1063/1.445869.

123. Case, D.A., Aktulga, H.M., Belfon, K., Cerutti, D.S., Cisneros, G.A., Cruzeiro, V.W.D., Forouzesh, N., Giese, T.J., Götz, A.W., Gohlke, H., et al. (2023). AmberTools. Journal of Chemical Information and Modeling *63*, 6183-6191. 10.1021/acs.jcim.3c01153.

124. Wei, D., Huang, X., Qiao, Y., Rao, J., Wang, L., Liao, F., and Zhan, C.-G. (2017). Catalytic Mechanisms for Cofactor-Free Oxidase-Catalyzed Reactions: Reaction Pathways of Uricase-Catalyzed Oxidation and Hydration of Uric Acid. ACS Catalysis *7*, 4623-4636. 10.1021/acscatal.7b00901.

125. Neese, F. (2012). The ORCA program system. WIREs Computational Molecular Science *2*, 73-78. 10.1002/wcms.81.

126. Neese, F. (2018). Software update: the ORCA program system, version 4.0. WIREs Computational Molecular Science *8*, e1327. https://doi.org/10.1002/wcms.1327.

127. Bannwarth, C., Caldeweyher, E., Ehlert, S., Hansen, A., Pracht, P., Seibert, J., Spicher, S., and Grimme, S. (2021). Extended tight-binding quantum chemistry methods. WIREs Computational Molecular Science *11*, e1493. 10.1002/wcms.1493.

128. Bannwarth, C., Ehlert, S., and Grimme, S. (2019). GFN2-xTB—An Accurate and Broadly Parametrized Self-Consistent Tight-Binding Quantum Chemical Method with Multipole Electrostatics and Density-Dependent Dispersion Contributions. Journal of Chemical Theory and Computation *15*, 1652-1671. 10.1021/acs.jctc.8b01176.

129. Larkin, M.A., Blackshields, G., Brown, N.P., Chenna, R., McGettigan, P.A., McWilliam, H., Valentin, F., Wallace, I.M., Wilm, A., Lopez, R., et al. (2007). Clustal W and Clustal X version 2.0. Bioinformatics (Oxford, England) *23*, 2947-2948. 10.1093/bioinformatics/btm404.

Langtaosha (LTS) Preprint doi: https://doi.org/10.65215/LTSpreprints.2026.04.18.000189. This version posted April 18, 2026. The copyright holder for this preprint (which was not certified by peer review) is the author/funder. Creative Commons license: CC Attribution-NonCommercial-NoDerivatives 4.0 https://creativecommons.org/licenses/by-nc-nd/4.0

130. Robert, X., and Gouet, P. (2014). Deciphering key features in protein structures with the new ENDscript server. Nucleic Acids Research *42*, W320-W324. 10.1093/nar/gku316.

131. Camacho, C., Coulouris, G., Avagyan, V., Ma, N., Papadopoulos, J., Bealer, K., and Madden, T.L. (2009). BLAST+: architecture and applications. BMC bioinformatics *10*, 421. 10.1186/1471-2105-10-421.

132. Goldfarb, T., Kodali, V.K., Pujar, S., Brover, V., Robbertse, B., Farrell, C.M., Oh, D.-H., Astashyn, A., Ermolaeva, O., Haddad, D., et al. (2025). NCBI RefSeq: reference sequence standards through 25 years of curation and annotation. Nucleic Acids Research *53*, D243-D257. 10.1093/nar/gkae1038.

133. Edgar, R.C. (2004). MUSCLE: multiple sequence alignment with high accuracy and high throughput. Nucleic Acids Research *32*, 1792-1797. 10.1093/nar/gkh340.

134. Hinchliff, C.E., Smith, S.A., Allman, J.F., Burleigh, J.G., Chaudhary, R., Coghill, L.M., Crandall, K.A., Deng, J., Drew, B.T., Gazis, R., et al. (2015). Synthesis of phylogeny and taxonomy into a comprehensive tree of life. Proceedings of the National Academy of Sciences *112*, 12764-12769. 10.1073/pnas.1423041112.

135. Michonneau, F., Brown, J.W., and Winter, D.J. (2016). rotl: an R package to interact with the Open Tree of Life data. Methods in Ecology and Evolution *7*, 1476-1481. 10.1111/2041-210X.12593.

136. Xu, S., Li, L., Luo, X., Chen, M., Tang, W., Zhan, L., Dai, Z., Lam, T.T., Guan, Y., and Yu, G. (2022). Ggtree: A serialized data object for visualization of a phylogenetic tree and annotation data. iMeta *1*, e56. 10.1002/imt2.56.